Check for updates

Received: 17 July 2023 | Revised: 6 December 2023 | Accepted: 6 January 2024

DOI: 10.1002/pip.3778

RESEARCH ARTICLE

Composition dependence of electronic defects in $CuGaS_2$

Damilola Adeleye | Mohit Sood | Michele Melchiorre | Alice Debot | Susanne Siebentritt

Laboratory for Photovoltaics, Department of Physics and Materials Science, University of Luxembourg, Belvaux, Luxembourg

Correspondence
Damilola Adeleye and Susanne Siebentritt, Laboratory for Photovoltaics, Department of Physics and Materials Science, University of Luxembourg, Belvaux L-4422, Luxembourg.
Email: damilola.adeleye@uni.lu; susanne.siebentritt@uni.lu

Funding information
Luxembourg National Research Fund (FNR), Grant/Award Number: PRIDE 15/10935404

Abstract

$CuGaS_2$ films grown by physical vapor deposition were studied by photoluminescence (PL) spectroscopy, using excitation intensity and temperature-dependent analyses. We observed free and bound exciton recombinations, three donor-to-acceptor (DA) transitions, and deep-level transitions. The DA transitions at ~2.41, 2.398, and ~2.29 eV are attributed to a common donor level ~35 meV and two shallow acceptors at ~75 and ~90 meV and a deeper acceptor at 210 meV above the valence band. This electronic structure is similar to those of other chalcopyrite materials. The observed DA transitions are accompanied by several phonon replicas. The Cu-rich and near-stoichiometric $CuGaS_2$ films are dominated by transitions involving the acceptor at 210 meV. All films show deep-level transitions at ~2.15 and 1.85 eV due to broad deep defect bands. The slightly Cu-deficient films were dominated by intense transitions at ~2.45 eV, which were attributed to excitonic transitions, and a broad defect transition at 2.15 eV.

KEYWORDS

composition, $Cu(In,Ga)S_2$, $CuGaS_2$, $CuGaS_2$ solar cell, electronic defect, photoluminescence, quasi-Fermi level splitting, tandem

1 | INTRODUCTION

$Cu(In,Ga)S_2$ is not only a promising material for single-junction solar cells but also a strong candidate for top cells in tandem applications to absorb high-energy photons in the solar spectrum.[1–3] Barreau et al. reported an efficiency of 16%,[4] which is considerably lower than the efficiencies of the selenide chalcopyrites $Cu(In,Ga)Se_2$ which have reached 23.6% (M. Edoff et al., in preparation).[5] In particular, $Cu(In,Ga)S_2$ suffers from a high V_{OC} deficit.[6–10] This deficit is partly due to interface recombination, which can be mitigated by the correct choice of buffer layer, but also largely due to non-radiative recombination in the absorber bulk.[10] Therefore, it is essential to study the electronic defect structure of $CuGaS_2$. Selenide chalcopyrite $Cu(In,Ga)Se_2$, together with the ternaries $CuInSe_2$ and $CuGaSe_2$, has been intensively studied, and an understanding of the electronic structure and the impact of the composition has been established.[11–18] Accordingly, shallow donor and acceptor levels, as well as deep defects were, identified in both $CuInSe_2$ and $CuGaSe_2$. Spindler et al.[14] compared the wide-gap $CuGaSe_2$ with the low-gap $CuInSe_2$. For $CuGaSe_2$, it was reported that defect levels shift towards the mid-gap and defects that were shallow in $CuInSe_2$ become deeper in $CuGaSe_2$.[14] Thus, as Ga is substituted for In, shallow defects become deeper and form deep levels that serve as channels for unwanted non-radiative recombination in $Cu(In,Ga)Se_2$ absorbers.[11–14,19,20] The electronic defects in $Cu(In,Ga)S_2$, unlike their selenide counterparts, have been less studied.[21–25]

However, it has been shown that the shallow defects in ternary $CuInS_2$ are similar to those in selenide chalcopyrites, with three shallow acceptors and one shallow donor, plus two deep broad defect bands close to 0.8 and 1.1 eV.[9,26] For $CuGaS_2$, a comprehensive electronic

This is an open access article under the terms of the Creative Commons Attribution License, which permits use, distribution and reproduction in any medium, provided the original work is properly cited.
© 2024 The Authors. Progress in Photovoltaics: Research and Applications published by John Wiley & Sons Ltd.

defect structure is still incomplete.[27–34] To achieve high-efficiency sulfide-chalcopyrite solar cells, it is necessary to include Ga.[9] Therefore, it is essential to understand the structure of defects in $CuGaS_2$.

Previous reports on defects in $CuGaS_2$ have identified one or two donor-to-acceptor (DA) transitions at approximately 2.39–2.41 eV, which were attributed to a common shallow donor around 20–25 meV.[30,35] Earlier studies also reported shallow donor energy level of 45–50 meV.[27,28] In addition, deep-level transitions are observed at 2.1 eV and around 1.7 to 1.8 eV.[32,36] An additional deep transition ~2.3 eV was identified as either a DA transition or a deep defect.

In this study, photoluminescence (PL) spectroscopy was performed on $CuGaS_2$ films grown by physical vapor deposition to understand the electronic defect structure. We also report the performance of a solar cell fabricated on a Cu-rich $CuGaS_2$ absorber. A deeper understanding of the electronic defect structure of $CuGaS_2$ will enhance our understanding of the role of Ga in $Cu(In,Ga)S_2$ films and solar cells.

2 | EXPERIMENTAL DETAILS

2.1 | Deposition process for $CuGaS_2$ films

The polycrystalline $CuGaS_2$ films investigated in this work were deposited by one-stage co-evaporation of elemental Cu and Ga at source temperatures of ~1250°C and ~1150°C, respectively, under sulfur pressure between 5.9×10^{-5} and 8.5×10^{-5} mbar. Various compositions of $CuGaS_2$ films were obtained by changing the temperatures of the elemental sources and thus the elemental fluxes of Cu and Ga. The deposition was performed on Mo-sputtered high-temperature glass with better heat resistance than soda-lime glass[37] at an actual substrate temperature of ~690°C. Such a high substrate temperature is necessary to obtain high-quality Ga-containing films, particularly pure $CuGaS_2$.[38–40] This is partly due to (i) the slow elemental migration and reaction of Ga relative to In and the relatively high melting point of Ga-based samples compared to In-based samples,[38,41,42] as shown in the Cu_2S–In_2S_3 and Cu_2S–Ga_2S_3 phase diagrams.[38,42] (ii) The melting point of sulfides is higher than that of selenides because of the lower atomic radius of S compared to Se.[43–45]

The crystallinity, phases, and vibrational properties of the films were characterized by X-ray diffraction (XRD) using Cu-Kα radiation and Raman spectroscopy with an excitation wavelength of 532 nm. The surface morphology and cross-section micrographs were obtained using a scanning electron microscope (SEM), and the chemical composition was determined by energy-dispersive X-ray spectroscopy (EDX) with a beam energy of 20 kV on the as-grown films before etching. Therefore, the compositional ratio of the Cu-rich films mentioned in this report is an integration of the ternary chalcopyrite phase and secondary copper sulfide (Cu_xS) phase. As such, "Cu-poor" refers to material with a ratio [Cu]/[Ga] < 1, while "Cu-rich" refers to [Cu]/[Ga] > 1. The Cu-excess phases were removed by etching in an aqueous solution of 10% potassium cyanide (KCN) for 5 min.[46] After the etching procedure, the [Cu]/[Ga] ratio is approximately 1, that is, [Cu]/[Ga] = 0.98. Therefore, all the PL measurements were performed after KCN etching. It is well known from the selenide system that although the chalcopyrite phase is stoichiometric under Cu-rich growth, the observed defects still depend on the Cu-excess during growth.[47,48]

Lower substrate temperatures during the deposition of the $CuGaS_2$ films resulted in poor quality films with unidentifiable crystallographic phases among those close to $CuGa_3S_5$ and $CuGa_5S_8$.[49–51] This behavior is similar to that of $CuGaSe_2$ deposited at low temperatures.[52] Conversely, at these high deposition temperatures, group VI elements, such as sulfur and selenium, have low sticking coefficients and are extremely volatile, which increases the possibility and rate of sulfur loss and re-evaporation,[34,53–55] necessitating a high pressure of sulfur during growth. The growth parameters of four $CuGaS_2$ films grown at various sulfur vapor pressures and substrate temperatures, labeled G1–G4, are listed in Table 1.

Analysis of the chemical composition of film G1, deposited at an actual substrate temperature of 600°C and chamber pressure of 5.9×10^{-5} mbar, showed that the [S]/([Cu] + [Ga]) ratio was 0.7. The X-ray diffractogram in Figure 1 shows that the deficiency of sulfur in G1 promotes the growth of the γCu_9Ga_4 phase. Increasing the growth temperature to 620°C in G2 increased the S content and decreased the intensity of the γCu_9Ga_4 phase. Ultimately, by simultaneously increasing both the deposition temperature and chamber pressure to ~690°C and 5.9×10^{-5} mbar, respectively, the S content was increased to 1.0, and the unwanted γCu_9Ga_4 phase was suppressed. Hence, the deposition of $CuGaS_2$ requires a higher S overpressure[27] than that required for $CuInS_2$ or $Cu(In,Ga)S_2$[39,56] to mitigate sulfur loss. Consequently, during the $CuGaS_2$ deposition process, the sulfur pressure in the chamber was maintained in the range of 5.9×10^{-5} to 8.5×10^{-5} mbar. A deposition time of approximately 2 h was used to achieve a film thickness of approximately 2 μm.

2.2 | PL measurement

The PL measurements at low temperatures were conducted in a custom-designed system. A continuous-wave laser with a wavelength of 405 nm served as the excitation source. The excitation intensity, as

Film label	Actual substrate temperature	Sulfur pressure	[S]/([Cu] + [Ga])
G1	600°C	$3.7 \cdot 10^{-5}$ mbar	0.7
G2	620°C	$3.7 \cdot 10^{-5}$ mbar	0.7
G3	640°C	$4.7 \cdot 10^{-5}$ mbar	0.8
G4	690°C	$5.9 \cdot 10^{-5}$ mbar	1.0

TABLE 1 Influence of substrate temperature and sulfur pressure during deposition on the final sulfur content in different $CuGaS_2$ films after deposition.

1099159x, 0, Downloaded from https://onlinelibrary.wiley.com/doi/10.1002/pip.3778 by Cochrane Luxembourg, Wiley Online Library on [21/03/2024]. See the Terms and Conditions (https://onlinelibrary.wiley.com/terms-and-conditions) on Wiley Online Library for rules of use; OA articles are governed by the applicable Creative Commons License

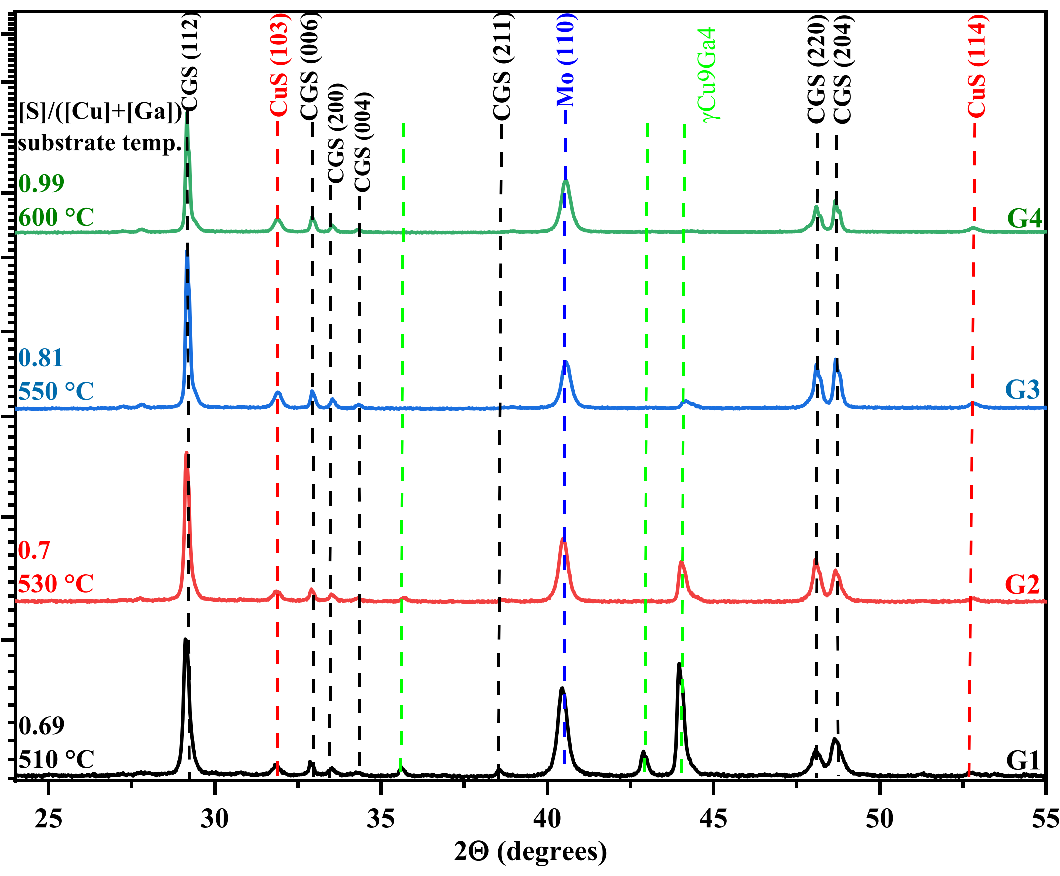

FIGURE 1 X-ray diffractograms of different $CuGaS_2$ films showing the effect of increasing the growth temperature and sulfur pressures in samples G1–G4. The diffraction peaks were identified using ICDD PDF 00-025-0279 and 01-085-1574 for $CuGaS_2$, 00-006-0464 for CuS, and 00-037-1492 for Mo.

determined by the photon flux, falls within the range of 10^{14}–10^{17} photons/cm^2/s. The measurements were conducted with the samples enclosed in a helium flow cryostat. To decrease the laser beam's spot size, a converging lens was positioned in front of the sample. The emissions from the samples were collected using two off-axis parabolic mirrors, which were then focused into either a 200- or 105-μm fiber. The PL emission was spectrally resolved by a monochromator and detected by either a Si charge-coupled device (CCD) or an InGaAs diode array. The grating and fiber used allow for a resolution of approximately 1–2 nm (0.002–0.004 meV), although at 1 nm there is a tradeoff between spectral resolution and the intensity of PL emission. A commercial light source with a known spectral distribution is employed to calibrate the PL setup and adjust the unprocessed data to account for the spectral characteristics of the setup. During the data-acquisition process, a long exposure time was employed to gather raw data with minimal noise. To conduct excitation intensity-dependent measurements, the laser power was adjusted and attenuated with the aid of different neutral-density filters. To determine the quasi-Fermi level splitting (QFLS) of the films, intensity-calibrated PL measurements were carried out at room temperature. The QFLS of the films was calculated by assessing their external radiative efficiency at a photon flux density comparable to 1 sun.[57] The bandgap of the absorbers was determined on the basis of the maximum intensity of the PL peak.

3 | EFFECT OF GROWTH CONDITIONS ON THE STRUCTURAL PROPERTIES OF THE FILMS

Before presenting the results and discussing the optical characterization of different spectral regions on the films, it is imperative to ascertain the quality of the films under investigation. Hence, in the following section, material characterization in terms of composition analyses, preferential chalcopyrite orientation, crystallinity, and microstructural properties obtained from SEM–EDX, XRD, and Raman analyses will be examined.

The chemical composition of the different films studied, as analyzed by EDX, is between 0.94 and 1.8 in [Cu]/[Ga] atomic ratio. Figure 2 shows SEM micrographs depicting the typical surface morphology and cross-sectional images of Cu-rich and Cu-poor films. The specific chemical compositions of the fims are [Cu]/[Ga] = 1.3 for the Cu-rich film, and [Cu]/[Ga] = 0.94 for the Cu-poor film. The micrographs were obtained after the Cu_xS secondary phase was etched

1099159x, 0, Downloaded from https://onlinelibrary.wiley.com/doi/10.1002/pip.3778 by Cochrane Luxembourg, Wiley Online Library on [21/03/2024]. See the Terms and Conditions (https://onlinelibrary.wiley.com/terms-and-conditions) on Wiley Online Library for rules of use; OA articles are governed by the applicable Creative Commons License

FIGURE 2 SEM micrographs showing the microstructures of $CuGaS_2$ films. Top view and topographical view of a typical (etched) Cu-rich film (A,C) and Cu-poor film (B,D).

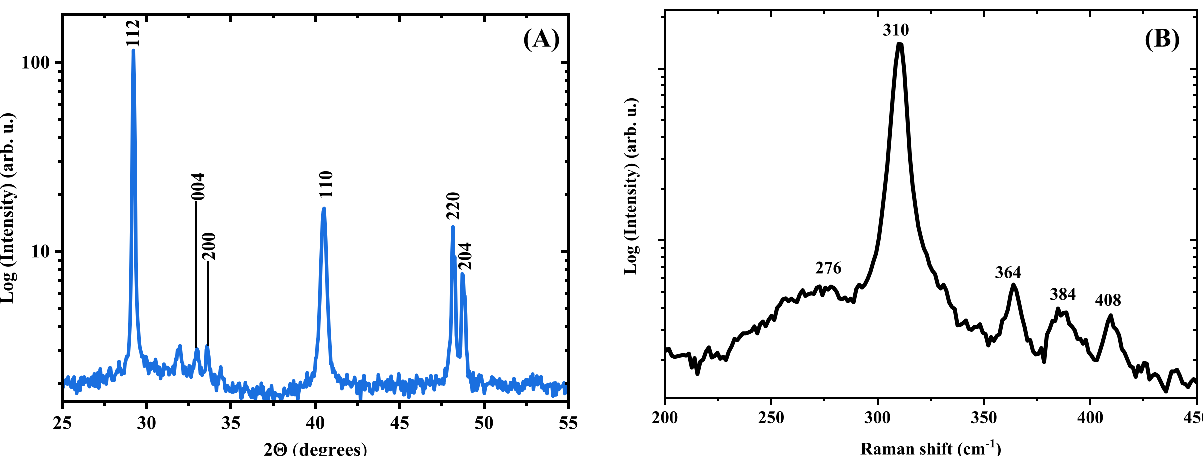

FIGURE 3 (A) The X-ray diffractogram of the as-grown Cu-rich $CuGaS_2$ film in Figure 2. (B) Raman spectrum of the Cu-rich $CuGaS_2$ film.

using a 10% KCN solution. The top view (Figure 2B) and cross-sectional images (Figure 2D) of the Cu-poor film show a rough granular surface with pyramidal grains that are compact and well-connected to the back on the Mo back contact. On the other hand, the micrographs in Figure 2A,C show that the Cu-rich films featured smoother surfaces with larger and denser grains. This is in accordance with other chalcopyrite compounds, where it is well established that Cu-excess promotes the formation of large grain sizes and improves crystallinity.[58–62] Additionally, the high deposition temperature and pressure could have contributed to the quality of both Cu-rich and Cu-poor films, as these conditions foster effective nucleation and improve the quality of grain growth.[34,37]

The characteristic crystallographic orientation of the prevalent phase in the layers obtained from the X-ray analysis is shown in the diffractogram in Figure 3A. The ICDD database (00-025-0279) was used as a reference to index the peaks. The most prominent peak is the (112) plane of $CuGaS_2$. The peak at 41° in Figure 3A is due to the Mo back contact. A measure of the crystal quality was manifested in the splitting of the 220 and 204 peaks, resulting from the tetragonal distortion occurring in the chalcopyrite unit cell. The crystal quality of the films investigated was also corroborated by the absence of secondary phases, as shown in Figure 3A, in addition to the Cu_xS phases expected in a Cu-rich film. Figure 3B shows the Raman spectrum of a Cu-rich $CuGaS_2$ film. The dominant line at 310 cm^{-1} is the A1 mode, which corresponds to the vibration of the sulfur (or group VI) atom.[63,64] This mode is also the dominant Raman mode in other chalcopyrite compounds such as $CuInS_2$, $CuInSe_2$, and $CuGaSe_2$.[65,66]

1099159x, 0, Downloaded from https://onlinelibrary.wiley.com/doi/10.1002/pip.3778 by Cochrane Luxembourg, Wiley Online Library on [21/03/2024]. See the Terms and Conditions (https://onlinelibrary.wiley.com/terms-and-conditions) on Wiley Online Library for rules of use; OA articles are governed by the applicable Creative Commons License

The other less intense but notable Raman-active modes appearing at 276, 364, and 384 cm^{-1} correspond to the highest longitudinal optical phonon modes,[63] whereas the peak at 408 cm^{-1} was attributed to MoS_2.[67] The impact of the modes is revisited in relation to the observed phonon replicas in the PL spectra, as discussed in the subsequent section. However, the absence of any characteristic secondary phases indicates the high quality of the $CuGaS_2$ film. In summary, the results from the SEM–EDX, XRD, and Raman analyses indicates the high quality of the $CuGaS_2$ films.

4 | PL FEATURES OF $CuGaS_2$ AT LOW TEMPERATURE

First, a summary of the PL spectra of $CuGaS_2$ with varying compositional ratios is presented together with the assignment of the observed transitions. Subsequently, the methods used to analyze and assign different peaks to a specific transition are discussed. Figure 4 shows an overview of the different $CuGaS_2$ PL spectra by

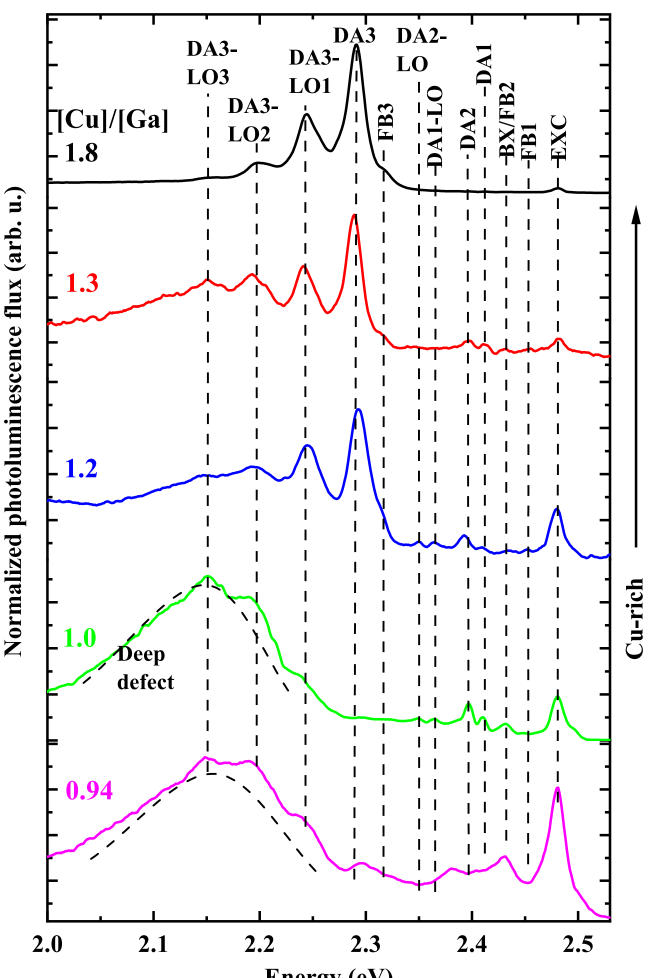

FIGURE 4 Photoluminescence spectra of $CuGaS_2$ with different chemical compositions at 10 K. The attribution of the peaks to the transitions in the figure is presented in the following sections.

composition at 10 K. The spectra feature (i) near-band-edge emissions with sharp intense excitonic (EXC) peaks around 2.48, 2.49, and 2.502 eV; (ii) shallow defect-related emissions between 2.25 and 2.45 eV: several free-to-bound (FB) and DA transitions with their phonon replicas; and (iii) a broad deep defect peak at ~2.15 eV. The influence of the [Cu]:[Ga] composition on some peaks can be clearly observed in the 2.3 eV transition (DA3), where the relative intensity of the peak increases with increasing Cu content, even dominating and screening other peaks in the spectrum for the film with a [Cu]/[Ga] ratio of 1.8.

For slightly Cu-rich films with a [Cu]/[Ga] ratio of 1.3, for example, the relative intensity of the 2.3 eV transition to the other peaks decreases, and it is noticeable that the 2.3 eV transition overlaps with the broad peak around 2.15 eV. In contrast, the intensity of the broad peak at ~2.15 eV and another at 1.85 eV (Figure 16) increases with lower Cu content, and it dominates the Cu-poor material alongside the EXC transition at 2.48 eV and transitions around 2.40 eV.

To investigate the different spectral regions, the relative intensities of the transitions described above were considered, and the near-band-edge emissions and shallow defects were investigated using the near-stoichiometric and Cu-rich films, whereas the deep defects were studied with Cu-poor and near-stoichiometric films. The assignment of a peak to a specific transition follows the evaluation of the PL flux dependence on the excitation intensity on a double-logarithmic scale, and the energy position on the excitation intensity on a semi-logarithmic scale.[68] In this report, the PL flux and energy position was obtained from Gaussian fit of the PL spectra. However, DA transitions are better fitted by a Poisson distribution using the Huang–Rhys model as shown in Equation (6). The high luminescence of some samples allowed for a wide range of excitation intensities over many orders of magnitude, and the double-logarithmic plot of the excitation-dependent integrated PL flux of such samples resulted in a curvature that could not be described by a single power law.

The curvature is inherent and occurs when multiple defect levels participate in the recombination process.[69] Using rate equations and charge balance, exhaustive conditions beyond the simple case, where a single power law can describe the PL flux dependence on excitation intensity, were reported in previous studies.[69–71] A more comprehensive double power-law expression that better describes the curved shape is,

$$I_{PL} \propto \frac{\phi^{k_1+k_2}}{1+\left(\frac{\phi}{\phi_0}\right)^{k_1}}, \quad (1)$$

where k_i ($i=1$, 2) takes on multiples of $\frac{1}{2}$ and ϕ_0 is a turning point or crossover excitation at which a state involved in the recombination process becomes saturated.[69] Essentially, for a curved double-log plot, the k values for exciton-related transitions are between $\frac{2}{2} \le k \le \frac{4}{2}$, whereas they are between $\frac{1}{2} \le k \le \frac{3}{2}$ for defect-related transitions.[69] A simple summary of the k values for different transitions investigated in this work is presented in Table 2; however, more complex cases can be found in Spindler et al.[69] and Schmidt et al.[70]

1099159x, 0, Downloaded from https://onlinelibrary.wiley.com/doi/10.1002/pip.3778 by Cochrane Luxembourg, Wiley Online Library on [21/03/2024]. See the Terms and Conditions (https://onlinelibrary.wiley.com/terms-and-conditions) on Wiley Online Library for rules of use; OA articles are governed by the applicable Creative Commons License

TABLE 2 Summary of the behavior of the power-law exponent (k value) and β values with respect to the excitation intensity.

Type of transition	Power-law exponent (k) Low (ϕ)	High (ϕ)	Change of energy position (β value)
Exciton	$\frac{4}{2}$	$\frac{2}{2}$	0
Donor-to-acceptor (DA)	$\frac{3}{2}$	$\frac{1}{2}$	1–5 meV/decade
Free-to-bound (FB)	$\frac{3}{2}$	$\frac{1}{2}$	0

Note: The k values are multiples of $\frac{1}{2}$.

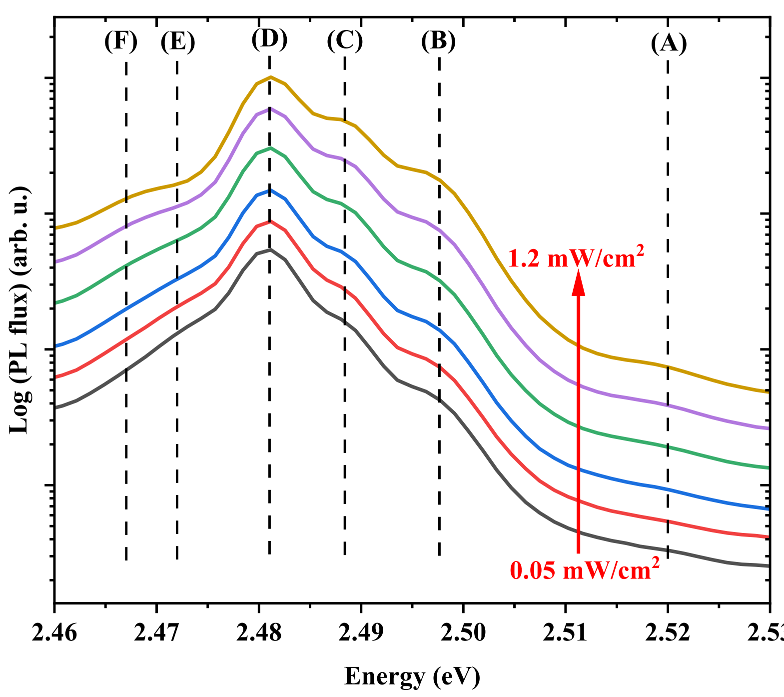

FIGURE 5 Near-band-edge spectra of Cu-rich $CuGaS_2$ measured at 10 K at several excitation intensities. The energy positions of the transition peaks are 2.518 (A), 2.496 (B), 2.488 (C), 2.481 (D), ~2.474 (E), and 2.468 eV (F). The dashed lines highlight the constant energy positions with increasing excitation intensity.

To distinguish between DA and FB transitions, we used the characteristic blue shift of the emission energy of DA transitions with increasing excitation intensity.[68,72] This energy position is expressed by

$$E_{DA} = E_G - (E_D + E_A) + \frac{q^2}{4\pi\varepsilon_0\varepsilon_r R_{DA}}, \quad (2)$$

where E_{DA} is the energy position of the DA transition, E_G is the bandgap, E_D is the donor defect energy relative to the conduction band, and E_A is the acceptor defect energy relative to the valence band. The term on the right is the Coulomb energy, with q being the elementary charge, ε_0 is vacuum permittivity, ε_r is the relative permittivity, and R_{DA} is the spatial distance between the donor and acceptor.[68,73] As the excitation intensity increased, the density of neutralized donors and acceptors increased and the spatial distance R_{DA} between the donor and acceptor atoms decreased, thereby increasing the influence of the Coulomb interaction. The relationship between the transition energy position in dependence of excitation intensity is empirically described by

$$E_{DA}(\phi) \propto E_{DA}(\phi_0) + \beta \log\left(\frac{\phi}{\phi_0}\right), \quad (3)$$

where β typically takes values between 1 and 5 meV per decade of excitation intensity.[74]

4.1 | Near-band-edge luminescence of $CuGaS_2$ (2.46–2.53 eV)

The band-edge emissions were assessed using the film with the highest Cu content with a [Cu]/[Ga] ratio of 1.8, owing to its high luminescence flux and well-resolved peaks, although not obvious in Figure 4, because of the high luminescence of the DA3 transition. The luminescence strength of this film also supports the enhanced crystallinity when the material is processed under a high Cu excess. A plot of the PL spectra in the near-band-edge region between 2.46 and 2.53 eV at different excitation intensities is illustrated in Figure 5. We argue that the emission line B is the ground state of the free exciton, whereas A is the first excited state. Lines C–F are identified as bound excitons. It should be stated that biexciton luminescence[75] has been reported in this energy rather; however, this possibility was not investigated in this report.

Of the six peaks delineated, the most intense peak was at ~2.481 eV (D), with transitions at 2.488 eV (C) and 2.496 eV (B) at

1099159x, 0, Downloaded from https://onlinelibrary.wiley.com/doi/10.1002/pip.3778 by Cochrane Luxembourg, Wiley Online Library on [21/03/2024]. See the Terms and Conditions (https://onlinelibrary.wiley.com/terms-and-conditions) on Wiley Online Library for rules of use; OA articles are governed by the applicable Creative Commons License

lower intensities, but was visible in all spectra. At the high-energy end, the weak line at ~2.518 eV (A) was visible only at high excitation. At the low-energy end, the intensity of the transition at ~2.474 eV (E) decreased, whereas the 2.468 eV (F) peak is more resolvable at higher excitation intensities. In Figure 5, the lines do not show a shift in energy position with increasing excitation intensity, which preliminarily leaves them as either EXC or FB transitions. To discriminate between these two possibilities, the PL flux with respect to the excitation intensity of the different peaks was evaluated using a double-log plot, as shown in Figure 6A. The multiple power law in Equation (1) was used to fit the curves, and the fit of the emission line at 2.496 eV (B) is presented in Figure 6B as an example.

The k exponent results in $\sim\frac{3}{2}$ at low excitation intensities and in $\sim\frac{2}{2}$ at high excitation intensities. As previously mentioned, the exponents take on multiples of $\frac{1}{2}$, and a change in the exponent occurs when competing transitions or a defect involved in the transition

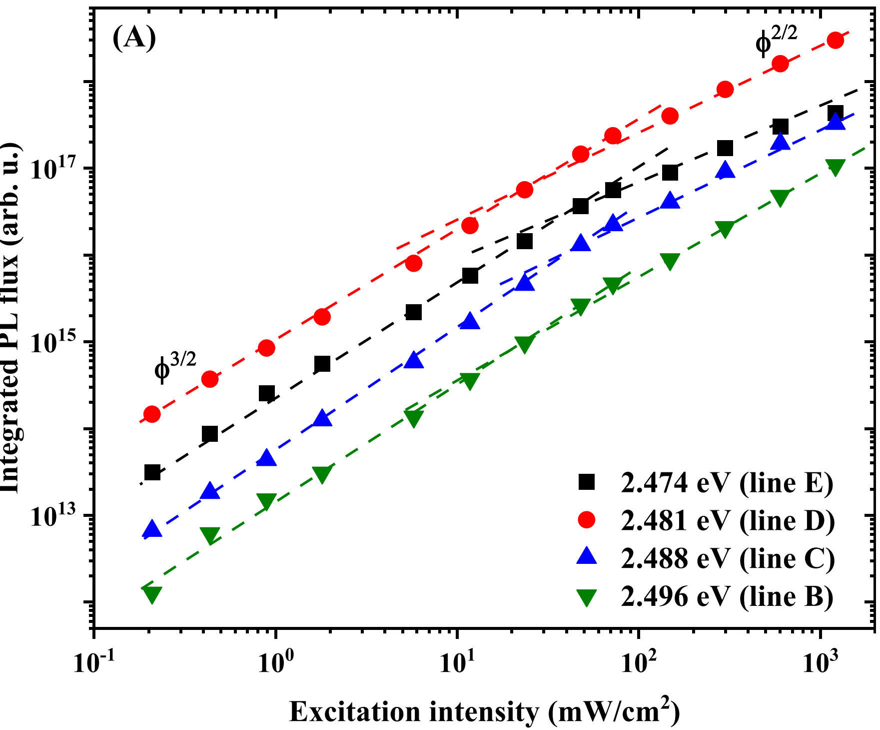

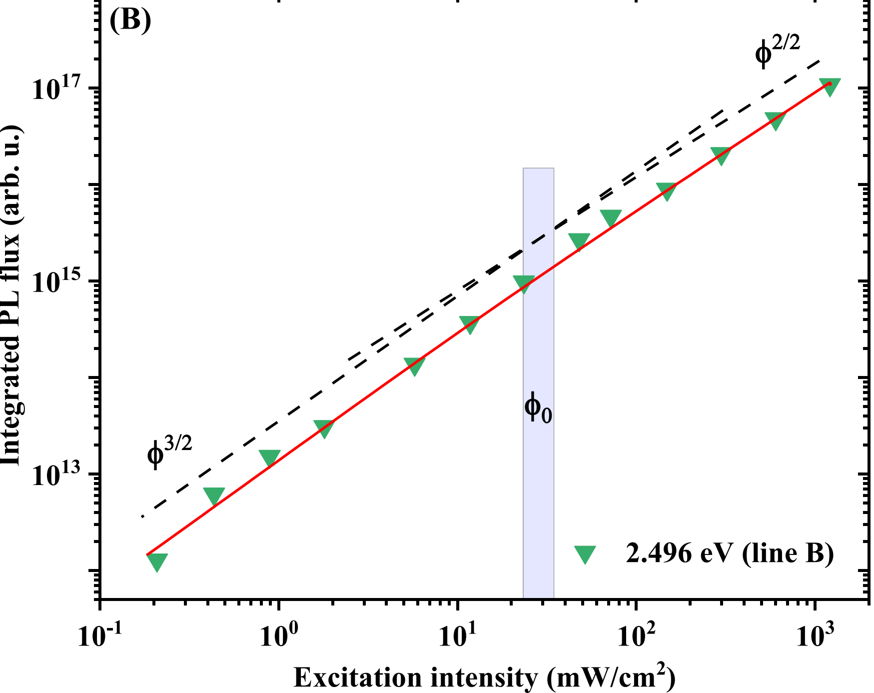

FIGURE 6 (A) Excitation intensity with respect to integrated PL flux for transition lines 2.474 (E), 2.481 (D), 2.488 (C), and 2.496 eV (B) fitted with the double power law. (B) Fit of emission line at 2.496 eV (B) with two power-law exponents $k=\frac{3}{2}$ and $k=\frac{2}{2}$ at high and low excitations, respectively. ϕ_0 denotes the turning point between the two excitation regimes, that is, the flux at which one of the defects is saturated.

1099159x, 0, Downloaded from https://onlinelibrary.wiley.com/doi/10.1002/pip.3778 by Cochrane Luxembourg, Wiley Online Library on [21/03/2024]. See the Terms and Conditions (https://onlinelibrary.wiley.com/terms-and-conditions) on Wiley Online Library for rules of use; OA articles are governed by the applicable Creative Commons License

saturates. The line B transition at 2.496 eV is attributed to the free exciton transition, because it occupies the highest energy position (apart from line A, which is only detected at a higher excitation intensity and will be discussed later). Bound excitons appear at lower energies owing to the larger binding energies of excitons to defects.[28,68,76] The attribution of line B to the free exciton is further substantiated by its subsequent use in deducing the free exciton binding energy (E_x) from the first excited state, as shown below.

In previous reports and in agreement with this report, free excitons were observed between 2.489 and 2.504 eV from photoreflectance spectroscopy and PL analyses.[28,31,77] In different reports, the disparity in the free exciton energy positions was linked to lattice strain and different analytical techniques.[54] The emission line A at 2.518 eV in Figure 6 matches the first excited state (n = 2) of the free exciton, and the free exciton binding energy can be determined from the energy-difference between the ground state $E_{FX}(n=1)$ and the first excited state $E_{FX}(n=2)$ using $E_x = \frac{4}{3}(E_{FX}(n=2) - E_{FX}(n=1))$.[68] The determined free exciton binding energy of 29 meV is in the range of the reported free exciton binding energy for $CuGaS_2$ between 28 and 32 meV,[28,36,78] which further justifies the designation of line A as the first excited state of the free exciton. This knowledge of E_X makes it possible to deduce the bandgap value at 10 K, which is important for determining the defect-level energies. Therefore, in this study, we report the corresponding bandgap ($E_g = E_{FX} + E_X$), for $CuGaS_2$ as 2.525 eV at 10 K.

For $CuGaS_2$, the hole effective mass (m_h) deduced from Hall-effect analysis and by calculation is 0.69 m_o,[79,80] where m_o is the electron mass, and the dielectric constant obtained from optical-absorption analysis is $\varepsilon_o = 8.5$.[81] Different values between 0.12 and 0.19 m_o have been reported for the reduced mass of $CuGaS_2$ by different groups; consequently, the electron effective mass (m_e) deduced from the reduced mass is between 0.13 and 0.26 m_o.[28,45,79,80,82] Therefore, the mass ratio (m_e/m_h) for $CuGaS_2$ is between 0.19 and 0.38. Sharma et al. found that the limit of mass ratio for a stable exciton bound to a charged donor and a charged acceptor is 0.20 and 0.29, respectively,[83] as such, the mass ratio for $CuGaS_2$ suggests that the binding of excitons to both ionized donors and acceptors in $CuGaS_2$ would result in unstable ionized complexes.[83]

However, binding energy for the neutral complex of both the donor $\left(D^0,X\right)$ and the acceptor $\left(A^0,X\right)$ can be found from the expressions

$$E_{(D^0,X)} = 0.12E_D + E_X, \quad (4)$$

$$E_{(A^0,X)} = 0.07E_A + E_X, \quad (5)$$

where E_D and E_A are the donor and acceptor energies, respectively.[28,83,84] Similar to the deduction of the binding energy of free excitons, the difference between a bound exciton and bandgap corresponds to the binding energy of the bound exciton.[85,86]

From the knowledge of the bandgap and exciton binding energy, the probable ionization energies of the donors or acceptors corresponding to an emission line can be calculated using Equations (4) and (5). The values are summarized in Table 3 for emission lines C to F. Previous reports have associated a similar transition to line C at 2.488 eV to a bound exciton recombination,[30,59] whereas other reports have attributed a comparable emission to the 2.481 eV line (D) as a FB recombination involving a transition between a neutral donor and the valence band edge.[59,87] According to the estimation presented in Table 3, it seems that the 2.488 eV exciton (C) is bound to a neutral acceptor at 67 meV or a neutral donor at 114 meV, whereas the 2.481 eV emission (D) is bound to a neutral donor at 125 meV or a neutral acceptor at 214 meV.

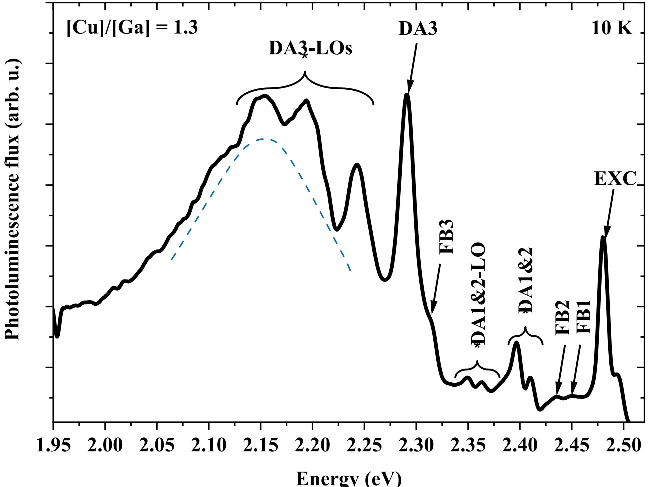

FIGURE 7 Low-temperature (10 K) spectrum of Cu-rich $CuGaS_2$ film with [Cu]/[Ga] of 1.3 measured at 0.2 mW/cm^2. Phonon replicas follow three DA transitions between 2.42 and 2.10 eV. The same film is shown in Figure 4 at a higher excitation intensity. The sample was chosen at this excitation power to highlight the appearance of several DA transitions and their replicas. The dashed line centered at approximately 2.15 eV delineates a broad transition around this energy.

TABLE 3 Estimated values of exciton binding energies and neutral donor and acceptor energy levels calculated using Equations (4) and (5) for emission lines C–F.

Line	Emission (eV)	Binding energy (meV)	Neutral donor E_D (meV)	Neutral acceptor E_A (meV)
C	2.488	37	67	114
D	2.481	44	125	214
E	2.474	51	183	314
F	2.468	57	233	400

1099159x, 0, Downloaded from https://onlinelibrary.wiley.com/doi/10.1002/pip.3778 by Cochrane Luxembourg, Wiley Online Library on [21/03/2024]. See the Terms and Conditions (https://onlinelibrary.wiley.com/terms-and-conditions) on Wiley Online Library for rules of use; OA articles are governed by the applicable Creative Commons License

1099159x, 0, Downloaded from https://onlinelibrary.wiley.com/doi/10.1002/pip.3778 by Cochrane Luxembourg, Wiley Online Library on [21/03/2024]. See the Terms and Conditions (https://onlinelibrary.wiley.com/terms-and-conditions) on Wiley Online Library for rules of use; OA articles are governed by the applicable Creative Commons License

The existence of either of these levels or the applicable levels is presented in the following sections. As shown below, the only shallow donor we find has a binding energy of 35 meV, which makes it unlikely that any of these excitons are bound to a donor. On the other hand, we found shallow acceptor states at energies near 100 and 200 meV, corresponding to bound excitons C and D. Additionally, we found several deep defects, which we can only speculate might be the defects to which the EXC E and F are bound.

Finally, in previous reports, transitions identical to line E were assigned to FB transition involving a shallow level.[27,28] However, excitation-dependent analyses of line E show that it exhibits exciton-related behavior. The consideration of the transitions at 2.474 (line E) and 2.468 eV (line F) as exciton-related transitions would require the excitons to be bound to a deep defect level, as inferred from Table 3.

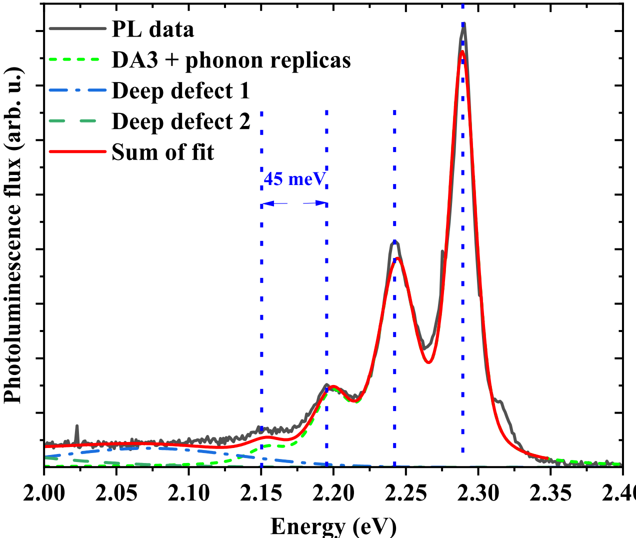

FIGURE 8 Low-temperature (10 K) PL spectrum of a $CuGaS_2$ film with [Cu]/[Ga] of 1.8 between 2.0–2.4 eV. The figure shows a fit of the phonon-assisted transition at ~2.29 eV (DA3) by Poisson function with consideration for deep defects. The low-intensity peak at ~2.32 eV is associated with an FB transition related to DA3, which will be discussed later.

4.2 | Shallow defects, DA-pair transitions, and phonon coupling

Several sharp peaks dominate the typical PL spectrum of Cu-rich $CuGaS_2$ at 10 K, between the range of 2.45 and 2.10 eV, as seen in Figures 4 and 7. Some of the peaks appear in groups at regular energy intervals, and as will be shown below, these are phonon replicas associated with shallow DA transitions. The series of sharp peaks follow an intense line known as the zero-phonon line (ZPL), which is followed at its low-energy end by several successive peaks of weakening intensities. These peaks are separated by the energy of the coupling LO-phonon. The excitation- and temperature-dependent behaviors of the phonon replicas were identical to the emission at the ZPL. As we show below, the spectral intensity of such phonon-assisted transitions is well described by the Poisson distribution expressed by

$$I_n \propto \exp(-S)\frac{S^n}{n!}, \tag{6}$$

where n is the number of phonons involved in the interaction, I_n is the intensity of the nth phonon replica, and S, known as the Huang–Rhys factor, is the coupling strength of the electron–phonon interaction of the corresponding defect.[88]

For shallow (weakly localized) defects, the electron–phonon coupling is weak and $S < 1$; thus, the ZPL is the most intense peak and does not shift in peak energy. However, if $S = 1$, the intensity of the first phonon replica is the same as that of the ZPL. Finally, if $S > 1$, there is a strong electron–phonon coupling of localized defects. This results in a shift of the maximum intensity away from the ZPL to a

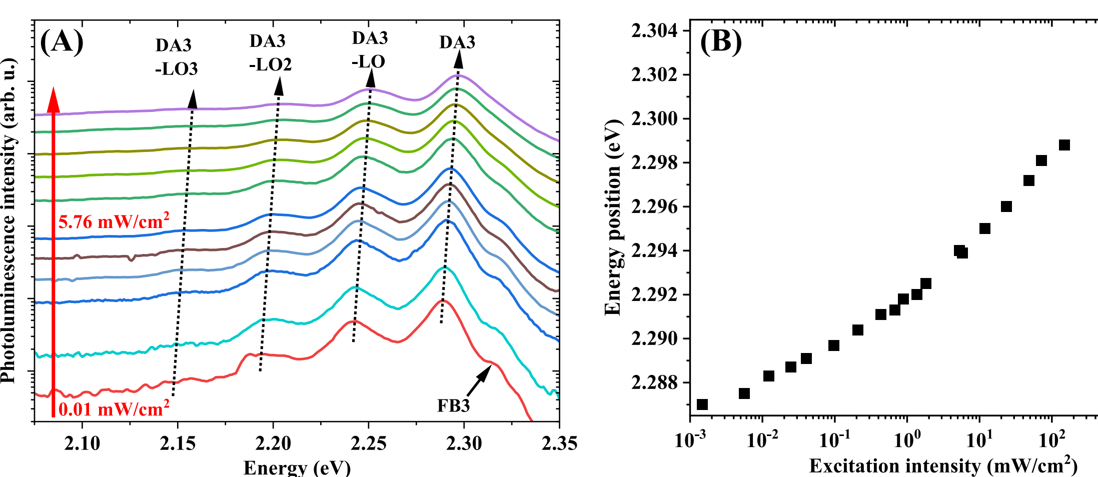

FIGURE 9 (A) Low-temperature (10 K) PL spectra of Cu-rich $CuGaS_2$ at different excitation intensities, demonstrating a shift in the energy position of DA3 and its phonon replicas with increasing excitation intensity. The dotted arrows are used to guide the eye for the shift in energy position. (B) Excitation intensity dependence of the energy position of DA3 transition in a semi-logarithm plot at 10 K.

lower energy because the phonon replicas have higher intensities than the ZPL. It is worth mentioning that for broadened emission bands, phonon replicas are not manifested by sharp peaks, but rather by a broad asymmetric distribution.[89–91]

In the following subsections, each of the DA pair transition peaks, as shown in Figure 7, that is, DA1, DA2, and DA3, along with their accompanying phonon replicas, are discussed. Additionally, the corresponding FB transitions at low temperatures are subsequently discussed.

4.2.1 | DA3 transition at ~2.29 eV

The low-temperature (10 K) PL spectrum showing the transition related to 2.29 eV, measured at a low excitation intensity, where the peaks were well resolved and without the strong influence of other defect peaks, is shown in Figure 8. The sample depicted in Figure 8 is the same as that displayed in Figure 4, with a [Cu]/[Ga] ratio of 1.8. Although the spectrum in Figure 8 was measured at an excitation intensity of 0.2 mW/cm^2, the spectrum in Figure 4 was measured at an excitation intensity of 5.76 mW/cm^2. The spectrum (Figure 8) features a series of peaks, with the most intense line at ~2.29 eV followed by several successive lines of weakening intensity at the low-energy end. These weakening lines are energy-spaced by ~45 ± 1 meV, corresponding to the lowest of the three highest energy optical phonon modes of 45.2, 47.6, and 49 meV,[63,92] which are equivalent to the Raman modes observed at the frequencies of 364, 384, and 408 cm^{-1} as seen in the Raman spectrum of $CuGaS_2$ presented in Figure 3B.

A fit of the spectral and intensity pattern by the Poisson distribution in Equation (6), while also considering a background of emissions from deep defects, yielded an S-factor of approximately 0.80 ± 0.05 and a ZPL at ~2.285 eV. This value of S and the energetic distance between the ZPL and the band gap are in agreement; for defect transitions more than 200 meV away from the bandgap, a rather high Huang–Rhys factor is expected.[68,90]

To identify the exact nature of the transition, the PL spectra acquired at different excitation intensities for the energy between 2.10 and 2.35 eV are presented in Figure 9A. It is evident that there is a blue shift of the peak positions for the ZPL and phonon replicas in parallel as the excitation intensity is increased. Such a shift in energy position is due to the influence of Coulomb interaction and is indicative of a DA transition as expressed by Equation (3).

The actual shift in the energy position can be extracted from the plot of the energy positions against the excitation intensity. As shown in Figure 9B, for the transition at ~2.29 eV, the plot of the energy position against the excitation intensity exhibits a curvature. This is due to the fact that, for a sufficiently wide range of excitation intensity, the energy positions of DA transitions assume an S-shape behavior.[69,93] The peak position approaches the energy position for infinite DA pair separation at the lowest excitation, whereas at the highest excitation, the peak position approaches the summation of infinite DA pair separation and the Coulomb energy for minimum DA pair separation.[93] The excitation dependence of the integrated PL flux for the DA3 transition is reported in the double-logarithmic plot shown in Figure 10. It can be observed that the plot in Figure 10 is a curvature that is adequately evaluated using Equation (1). A fit using two power-law exponents results in $k = \frac{2}{2}$ at low excitation intensity and $k = \frac{1}{2}$ at higher excitation intensity. The change in the exponent, referred to as crossover, occurred at approximately 3–6 mW/cm^2 of excitation intensity. This crossover indicates that a defect level or deeper mid-gap level interacting with the recombination process of the DA3 transition saturates at this intensity.[69]

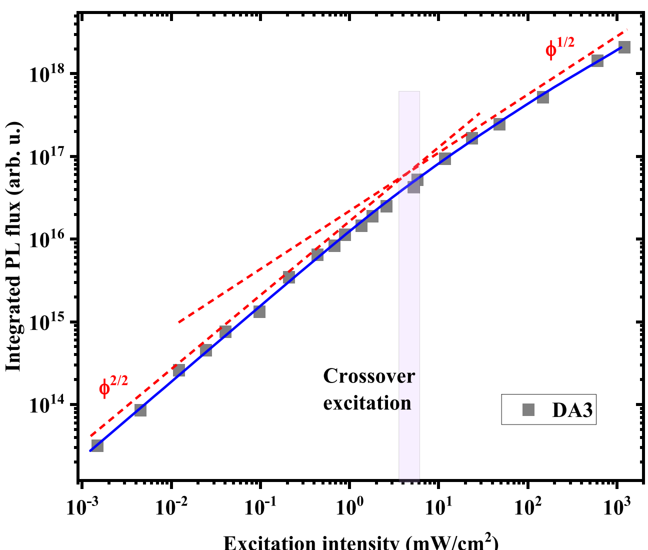

FIGURE 10 Double-logarithmic plot of the DA3 transition with integrated PL flux as a function of the excitation intensity. These values were extracted from the integrated PL flux of the Cu-rich $CuGaS_2$ spectra, as shown in Figure 9a.

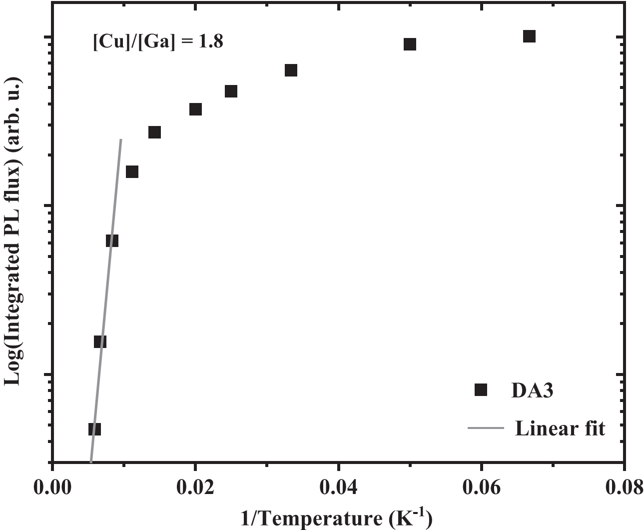

FIGURE 11 Arrhenius plot of the integrated PL flux with respect to temperature for thermal quenching of the DA3 transition in the Cu-rich $CuGaS_2$ film.

1099159x, 0, Downloaded from https://onlinelibrary.wiley.com/doi/10.1002/pip.3778 by Cochrane Luxembourg, Wiley Online Library on [21/03/2024]. See the Terms and Conditions (https://onlinelibrary.wiley.com/terms-and-conditions) on Wiley Online Library for rules of use; OA articles are governed by the applicable Creative Commons License

At the high-energy end of DA3 is a low-intensity peak at ~2.32 eV as seen in Figure 8 and 9A. The peak became more intense with increasing excitation intensity, as shown in Figure 9A, until it was eventually obscured by the broadening of the DA3 transition. Nevertheless, it is still noticeable in Figure 9A that the energy position barely changes with increasing excitation intensity. Given that the energy position of FB transitions does not shift with energy position, and owing to its proximity to the DA3 transition, the weak peak at ~2.32 eV is assigned FB3. It is noteworthy that the FB3 transition might account for the curvature of the excitation dependence of PL flux for DA3 as illustrated in Figure 10, since a shallow defect participating in the DA3 transition could saturate.[69] This is established by the value of the crossover excitation at ~3–6 mW/cm^2 in Figure 10 being close to the screening of FB3 in Figure 9A, as seen above in the PL spectrum at 5.76 mW/cm^2 in Figure 9A. Temperature-dependent analyses of the PL spectra shown in Figure 14 provided further support for the attribution of DA3 and FB3. It was observed that, as the temperature increased, the intensity of DA3 decreased, whereas the relative intensity of FB3 increased before thermal quenching of the transition.

This is another reason for associating this transition with FB3 because, ideally, a shallow defect involved in a DA transition is thermally emptied with increasing temperature, thus leaving the FB transition. The Arrhenius plot of Equation (7) of the integrated PL flux against the inverse temperature of thermal quenching of the DA3 transition is shown in Figure 11.

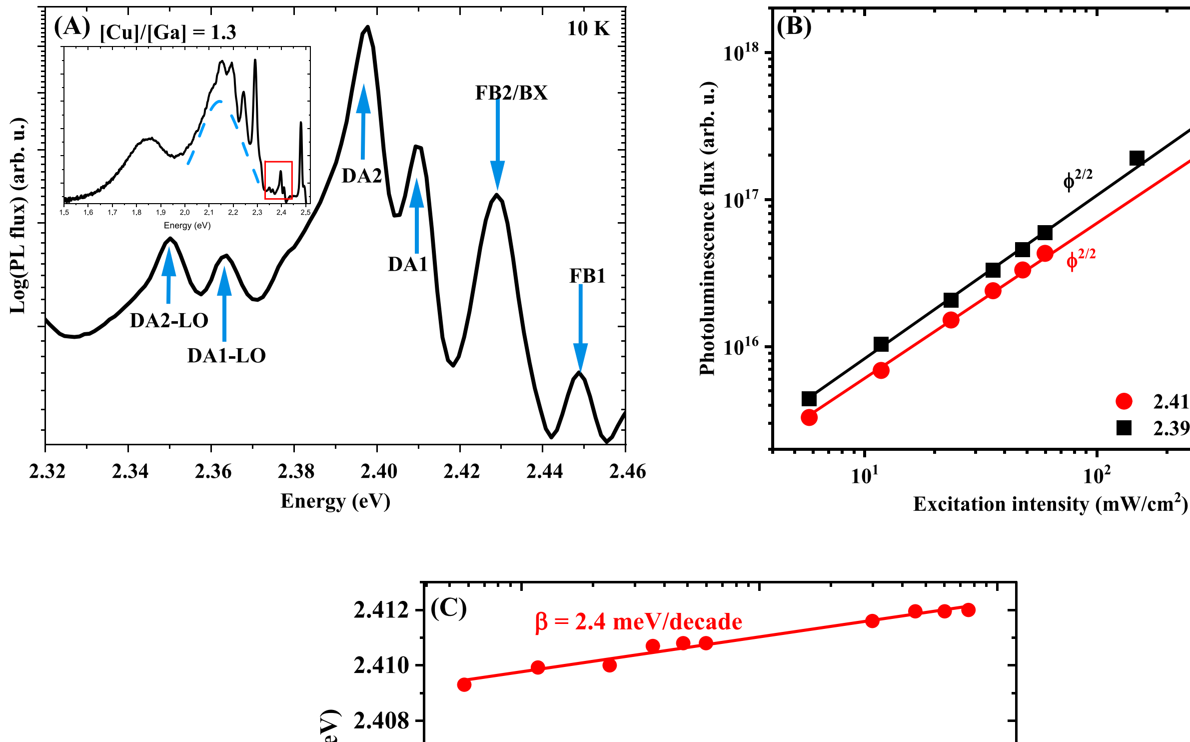

FIGURE 12 (A) Low-temperature (10 K) PL spectrum of Cu-rich $CuGaS_2$ measured at 0.9 mW/cm^2, showing phonon replicas accompanying the DA transitions at 2.410 (DA1) and 2.398 eV (DA2). The sample used to analyze the transitions was a $CuGaS_2$ film with a [Cu]/[Ga] ratio of 1.3, as shown in Figures 4 and 7. The inset in Figure 7 shows the full PL spectrum of the film. The dashed line centered at approximately 2.15 eV describes a broad transition related to a deep defect. The region of focus is indicated by a red box in the inset. (B) Integrated PL flux as a function of the excitation intensity of the 2.398 (DA2) and 2.410 eV (DA1) transitions at 300 K. (C) Excitation intensity dependence of the energy positions of the DA1 and DA2 transitions in a semi-logarithmic plot at 10 K.

1099159x, 0, Downloaded from https://onlinelibrary.wiley.com/doi/10.1002/pip.3778 by Cochrane Luxembourg, Wiley Online Library on [21/03/2024]. See the Terms and Conditions (https://onlinelibrary.wiley.com/terms-and-conditions) on Wiley Online Library for rules of use; OA articles are governed by the applicable Creative Commons License

$$I = \frac{I_0}{1 + C\exp^{\frac{-\varepsilon_0}{kT}}}. \tag{7}$$

The thermal activation energy was determined as ~35 ± 6 meV. This energy can be associated with the shallower defects involved in the DA transition, which is a donor, based on the lower effective mass of the electron. The energy difference between FB3 and DA3 was compatible with the emptying of the donor level at 35 meV. With the knowledge of the bandgap of 2.525 eV calculated for $CuGaS_2$ at 10 K, we derived the acceptor level of DA3 from the energy difference between FB3 and the bandgap as ~210 meV. Therefore, we conclude that DA3 is a transition between the donor level 35 meV below the conduction band and an acceptor level 210 meV above the valence band.

4.2.2 | DA1 and DA2 transitions around 2.40 eV

It will be shown in detail in the following, that below the band edge around 2.32–2.46 eV, two DA transitions are identified at 2.410 and 2.398 eV, followed at an energetic distance of ~46 meV by two peaks at 2.35 and 2.363 eV respectively, as shown in Figure 13A. Additionally, on the high-energy wing, two FB transitions were detected at ~2.43 and 2.45 eV. By fitting the DA lines with a Poisson distribution, the ZPLs were determined as 2.410 (DA1) and 2.398 eV (DA2). The Huang–Rhys factors were $S_{DA2} = 0.50 \pm 0.10$ and $S_{DA1} = 0.55 \pm 0.10$ for DA1 and DA2, respectively. These values are smaller than the S-factor for DA3 as expected, because the deeper the defect level, the more localized and tightly bound the carriers are to the defects; hence, an even stronger electron–phonon coupling.[90]

The integrated PL flux with respect to the excitation intensity presented in Figure 12B shows that both DA1 and DA2 can be fitted by a single power law, yielding an exponent $k \approx \frac{2}{2}$. As mentioned in the preceding section, k takes on multiples of $\frac{1}{2}$, and for DA transitions in particular, k approaches $\frac{2}{2}$ at low excitation intensities.[69] Additionally, the shift in the energy position for both DA1 and DA2 is ~2.4 meV/decade as shown in Figure 12C. Hence, it can be concluded that the DA1 and DA2 transitions in this study were within the limiting region of low excitation.

For the transitions at ~2.43 and 2.45 eV indicated as FB2/BX and FB1 respectively in Figure 12A, the integrated PL flux for both peaks with respect to excitation intensity in a double-log scale is shown in Figure 13A. The single power-law fit of both transitions also provided a power-law exponent $k = \frac{2}{2}$ for both transitions. This linear dependence of the PL flux on excitation intensity can be interpreted as transitions originating from DA at low excitation, FB transitions or BX transition,[68,69] although both transitions at ~2.43 and 2.45 eV have been tentatively reported as FB transitions.[30,31] The energy positions with respect to the excitation intensity, which are presented in Figure 13B, show no significant shift in the energy position with

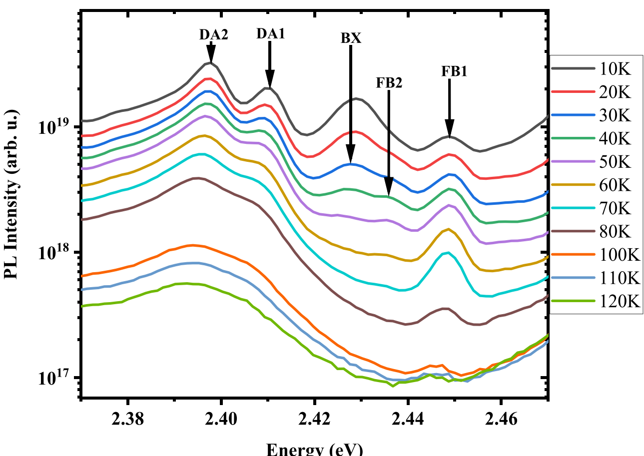

FIGURE 14 Temperature-dependent PL spectra of Cu-rich films with [Cu]/[Ga] ratio of 1.3. Temperature-dependent measurements led to the resolution of the bound exciton transition at 2.428 eV and free-to-bound peaks at 2.436 and 2.449 eV.

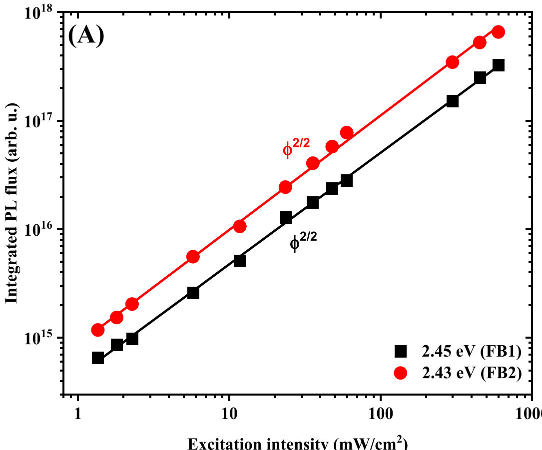

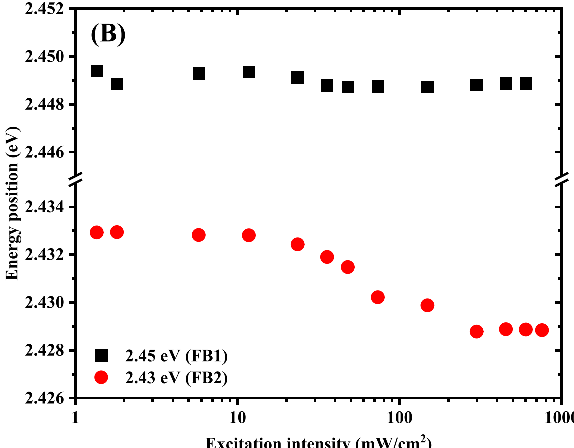

FIGURE 13 (A) PL flux in dependence of the excitation intensity for the transition peaks at 2.43 (FB2) and 2.45 eV (FB1). (B) Energy position in dependence of peak energy position for transitions at 2.43 and 2.45 eV.

1099159x, 0, Downloaded from https://onlinelibrary.wiley.com/doi/10.1002/pip.3778 by Cochrane Luxembourg, Wiley Online Library on [21/03/2024]. See the Terms and Conditions (https://onlinelibrary.wiley.com/terms-and-conditions) on Wiley Online Library for rules of use; OA articles are governed by the applicable Creative Commons License

increasing excitation intensity over three orders of magnitude for the 2.45 eV peak, making it an FB transition.

The behavior of the ~2.43 eV (FB2) transition in Figure 13B shows a shift in the energy position, that is, a shift from ~2.433 to ~2.428 eV. This phenomenon can be explained by the existence of two transitions occurring around 2.35 eV, that is, ~2.428 and 2.436 eV, which are better resolved by temperature-dependent analysis in Figure 14. Therefore, we conclude that, below the excitation intensity of 10 mW/cm^2 in Figure 13B, the 2.428 eV transition dominates; however, as the excitation intensity increases beyond 10 mW/cm^2, the intensity of the 2.436 eV transition increases and dominates. Hence, a shift in the energy position was observed, as shown in Figure 13B.

Temperature-dependent measurements were performed to understand the behavior of the DA1 and DA2 transitions and determine the influence of temperature on the associated FB or EXC transitions associated with DA1 and DA2. This is because shallow defects are thermally emptied with increasing temperature and contribute to the FB transitions.[68] The temperature-dependent spectra presented in Figure 14 show that as the temperature increased, the intensities of the DA1 and DA2 peaks decreased because the shallow defect levels involved in the transitions were thermally emptied. It becomes obvious that the 2.43 eV line (labeled FB2/BX in Figure 13A) consists of two peaks: one at 2.428 eV and the other at 2.436 eV. It was observed that the relative intensity of the 2.428 eV line (BX) rapidly decreased and was quenched at approximately 50 K, which is typical for a bound exciton. Its energy position suggests that it is bound to a much deeper defect than that of the excitons discussed above.

The relative intensities (compared to the DA transitions) of the 2.436 (FB2) and 2.448 eV (FB1) lines increased as the temperature increased up to 70 K before decreasing and quenching at 120 K, supporting their attribution as FB transitions. Given the proximity to the energy positions of DA1 (2.410 eV) and DA2 (2.398 eV), the transitions at 2.449 and 2.436 eV can be sufficiently associated with the DA1 and DA2 transitions as the related FB transitions at FB1 (2.449 eV) and FB2 (2.436 eV), respectively. Based on the energy difference between the DA and FB transitions, FB1 and FB2 appear to involve a common shallow donor at 35 meV. In accordance with the attribution of FB1 and FB2 and the estimated $CuGaS_2$ bandgap of 2.525 eV at 10 K, the 2.449 (FB1) and 2.436 eV (FB2) transitions were estimated to involve acceptor levels of approximately 75 and 90 meV, respectively.

At this point, in the analyses of the different transition peaks of $CuGaS_2$ studied in this report, a summary of the shallow defects in $CuGaS_2$ can already be drawn. The transitions DA1, DA2, and DA3 are assigned DA transitions due to the blue shift of their energy positions with excitation (β value) depending on the excitation intensity, and by the nature of their power-law exponents (k). For DA3, the power-law exponent changed from $k=\frac{2}{2}$ to $k=\frac{1}{2}$, whereas it was $k=\frac{2}{2}$ for both DA1 and DA2. In summary, there exists a common shallow donor (D1) level at ~35 meV, two shallow acceptor levels at

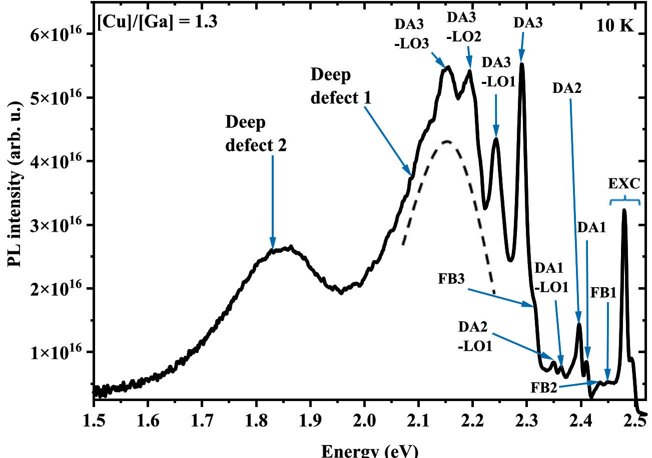

FIGURE 16 PL spectrum of Cu-rich $CuGaS_2$ at 10 K showing identified transitions.

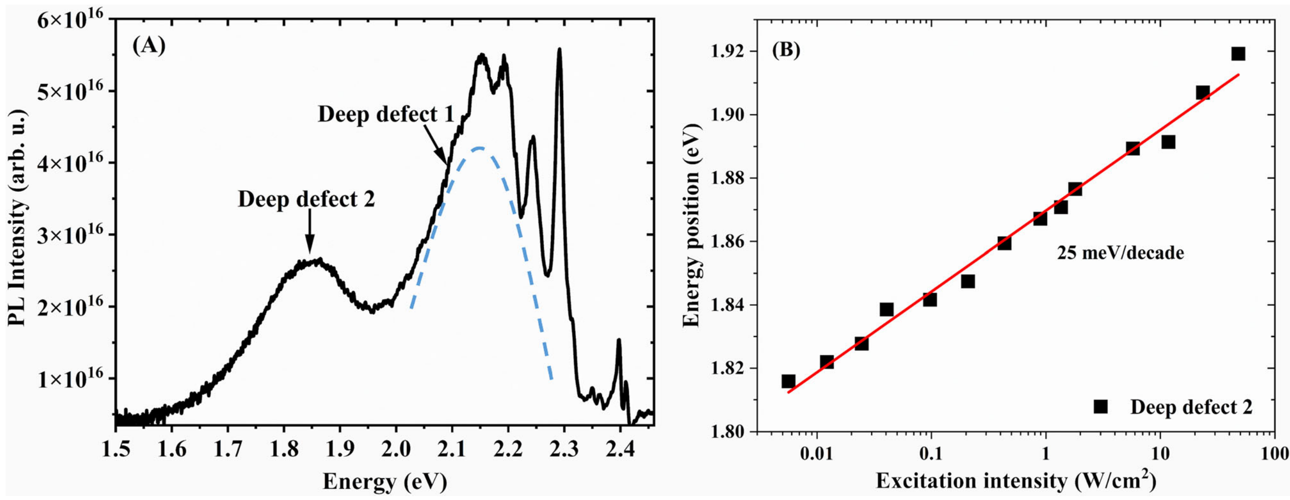

FIGURE 15 (A) Region of broadband deep defects featuring transitions centered at approximately 1.85 and 2.15 eV. (B) Energy position as a function of excitation intensity for deep defects at ~1.85 eV.

1099159x, 0, Downloaded from https://onlinelibrary.wiley.com/doi/10.1002/pip.3778 by Cochrane Luxembourg, Wiley Online Library on [21/03/2024]. See the Terms and Conditions (https://onlinelibrary.wiley.com/terms-and-conditions) on Wiley Online Library for rules of use; OA articles are governed by the applicable Creative Commons License

75 (A1) and 90 meV (A2), and an acceptor at 210 meV (A3). The tentative shallow defect levels involved in the DA1, DA2, and DA3 transitions are illustrated in Figure 18.

4.3 | Deep defects at 2.15 and 1.85 eV

The PL spectra of all the films (in Figure 4) investigated show that, as the compositional ratio of [Cu]/[Ga] decreases, the spectrum is dominated by two broad transitions in the range between 1.6 and 2.3 eV. The two transitions centered at 2.15 and 1.85 eV are as shown in Figure 15A. The occurrence of the transition at 2.15 eV is strongly composition dependent, as shown by the reports of Eberhardt et al.[33] and Botha et al.[36] Both groups reported that in Ga-rich samples, the transition shifts to ~2.0 eV, whereas in the Cu-rich samples, the transition shifts to higher energies of ~2.12–2.18 eV. Hence, it is possible that one or more defects are involved in the 2.15 eV transition, and this may account for the broadness of the peak. It is worth mentioning that in a Cu-poor film that is not presented in this report, it is possible to fit a peak at ~2.0 eV; hence, it is likely that there is an additional transition at ~2.0 eV. However, given that a Cu-rich film is used to investigate this peak in this report, the transition centered at 2.15 eV is in agreement with previous reports. Additionally, the phonon replicas on DA3 superpose on the 2.15 eV peak, thereby imposing constraints when fitting with an assumed Gaussian shape.

Analyses of the power-law dependence for both deep transitions yielded exponents of $k \sim 1$. The energy position with respect to the excitation intensity over four orders of magnitude shows a blue shift of ~5 meV per decade for the 2.15 eV peak, while the 1.85 eV peak shows a larger blue shift of ~25 meV per decade with respect to the excitation intensity, as presented in Figure 15B. Although the blue shift for the 2.15 eV transition is typical of a DA transition, the blue shift with 1.85 eV is much larger than expected for a DA transition. Therefore, in the past, the origin of the large blue shift was attributed to potential fluctuations in the band edges.[36] However, if the transition is broadened owing to potential fluctuations, all transitions will be broadened in the same manner. Therefore, potential fluctuations can be excluded as a source of the strong blue shift. Although it is apparent that both transitions likely involve a broad density of states, the large blue shift of the 1.85 eV transition might also be due to stronger phonon coupling manifested with deep defects.

4.4 | Summary and tentative defect levels in $CuGaS_2$

The PL spectra of slightly Cu-rich $CuGaS_2$ are summarized in Figure 16, with all peaks clearly identified. In the course of investigating the $CuGaS_2$ semiconductors in this report, several well-resolved exciton-related transitions were detected. The bandgap at 10 K was

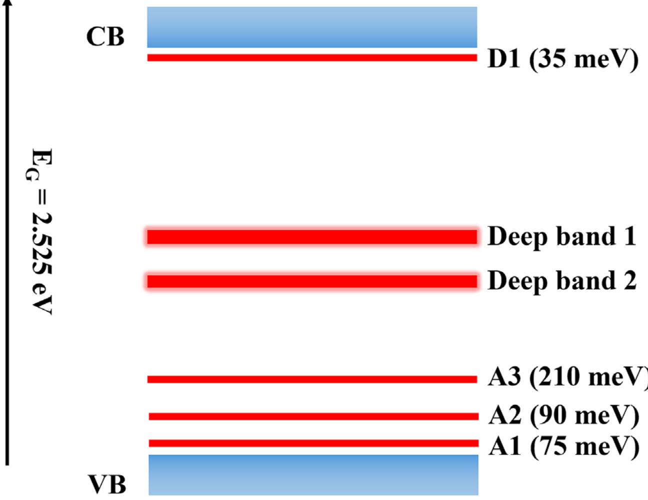

FIGURE 18 Tentative defect model for $CuGaS_2$ reported in this study. Two broad mid-gap defect levels are also assumed to be involved in the transitions in $CuGaS_2$.

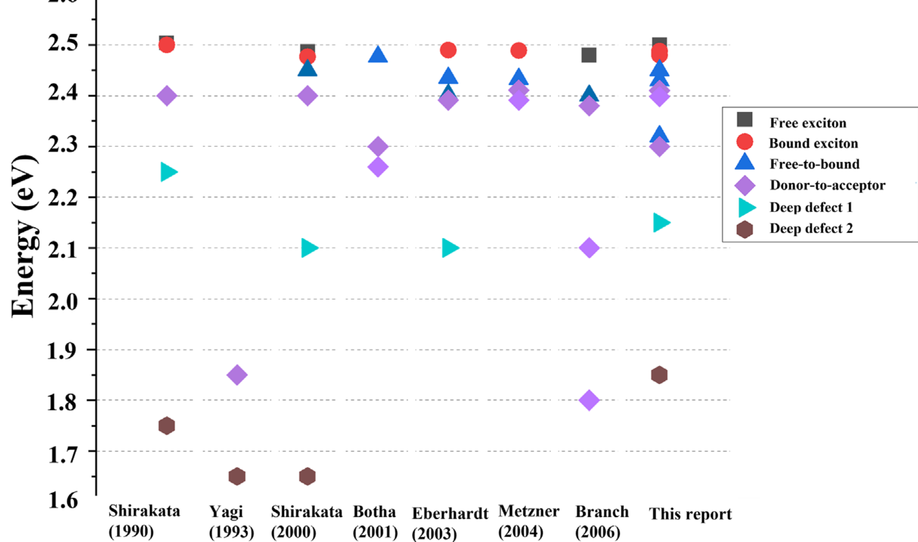

FIGURE 17 Overview of transition energies of $CuGaS_2$ from literature with transitions identified in this work.

1099159x, 0, Downloaded from https://onlinelibrary.wiley.com/doi/10.1002/pip.3778 by Cochrane Luxembourg, Wiley Online Library on [21/03/2024]. See the Terms and Conditions (https://onlinelibrary.wiley.com/terms-and-conditions) on Wiley Online Library for rules of use; OA articles are governed by the applicable Creative Commons License

determined to be 2.525 eV from the free exciton and its first excited state at 2.496 and 2.518 eV, respectively.

In this study, several sub-band-edge transitions were identified as DA transitions that interact with a common shallow donor level at 35 meV and shallow acceptors at 75 (A1) and 90 meV (A2). A deeper acceptor at 210 meV (A3) was also identified. In comparison with a previous report by Metzner et al., similar transitions and defect levels were reported: a shallow donor at 25 meV and two shallow acceptors at 89 meV and 109 meV were identified.[30] Furthermore, we observed that for the deeper acceptor A3, the related DA3 transition became more intense with higher Cu content. Botha et al. also reported similar defect level to A3 for slightly Cu-rich $CuGaS_2$[87]; an acceptor was identified at 210 meV above the valence band with a donor, likely at ~53 meV.[87] In this report, we conclude that DA1, DA2, and DA3 interact with a common shallow donor at 35 meV.

Finally, two broad transitions at 2.15 and 1.85 eV were present in all the films. Although both transitions are DA related, the exact defect levels involved require further investigations; however, both transitions presumably involve a broad density of states. Transitions involving these defects particularly dominate the PL spectrum of $CuGaS_2$ at room temperature.

In this study, we have identified a similar defect structure in $CuGaS_2$ as in $CuInSe_2$, $CuGaSe_2$,[11–14,19] and $CuInS_2$.[26,61] These structures feature three shallow acceptors and one shallow donor, although we found the third acceptor in $CuGaS_2$ to be deeper than in $CuInS_2$.[26,61] Furthermore, in the selenides, the shallow donor was around 10 meV whereas it is approximately 30 meV in $CuInS_2$.[11–14,19,26] In the selenides, it was reported that the three shallow acceptors become deeper when In is replaced with Ga.[14] A detailed comparison of the defect structure in sulfides and selenides has been reported by Siebentritt et al.[9]

An overview of the transition energies identified in literature and in this study is shown in Figure 17. Similar transition energies, independently reported by different research groups, were also identified in this study.

The tentative defect levels in $CuGaS_2$ are shown in Figure 18. The existence of a shallow donor level of ~35 meV (D1) and shallow acceptors of 75 (A1) and 90 meV (A2) with an additional deeper acceptor level at 210 meV (A3) were observed. Finally, the two deep transition levels appear to originate from two broad defect levels deep within the mid-gap.

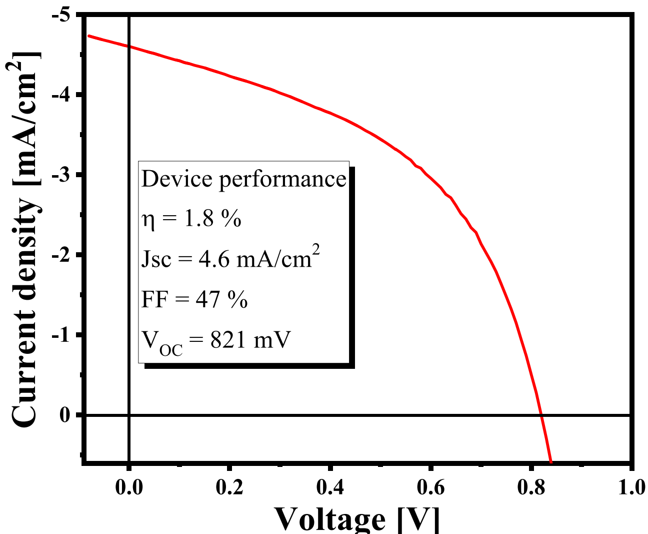

FIGURE 20 Current density–voltage curve of $CuGaS_2$ device prepared with (Zn,Mg)O buffer layer with Mg/(Mg + Zn) ~ 0.3 atomic percent.

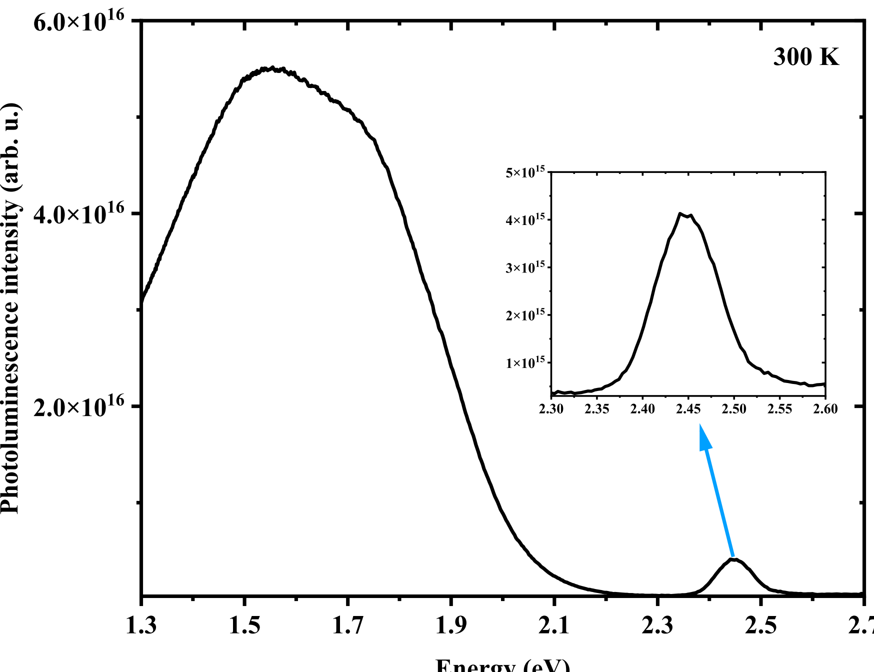

FIGURE 19 Room-temperature photoluminescence spectrum of $CuGaS_2$ absorber fabricated into a solar cell. The inset shows a magnification of the band-to-band transition.

1099159x, 0, Downloaded from https://onlinelibrary.wiley.com/doi/10.1002/pip.3778 by Cochrane Luxembourg, Wiley Online Library on [21/03/2024]. See the Terms and Conditions (https://onlinelibrary.wiley.com/terms-and-conditions) on Wiley Online Library for rules of use; OA articles are governed by the applicable Creative Commons License

5 | SOLAR CELL ON $CuGaS_2$ FILM

The room-temperature bandgap of $CuGaS_2$ is approximately 2.45 eV. Its wide bandgap makes it uninteresting for use as a single-junction solar cell. Nevertheless, it is important to understand how the defects in $CuGaS_2$ influence the electrical properties of single-junction solar cells. The absorber was a Cu-rich film with a [Cu]/[Ga] ratio of ~1.3. The room-temperature PL spectrum of the absorber is shown in Figure 19. The room-temperature spectrum is dominated by the broad transition centered around 1.5 eV as shown in Figure 19. The device possesses a QFLS of 1.68 eV, and consequently, a rather large deficit of 0.42 eV compared to the Shockley–Queisser open-circuit voltage $\left(V_{OC}^{SQ}\right)$[94] owing to the defects in the material. The QFLS was determined by evaluating the PL quantum efficiency of the absorber to determine the non-radiative loss or limiting factor from the ideal value.[57]

The current density–voltage characteristics of the $CuGaS_2$ device with a (Zn,Mg)O buffer layer, an Al:ZnMgO sputtered i-layer, and an Al:ZnO window layer are shown in Figure 20. The device demonstrated a V_{OC} of 821 mV, leading to a very high interface V_{OC} deficit[95] compared to its QFLS. Consequently, the power conversion efficiency was only 1.8%. We speculate that the high interface V_{OC} deficit originates from two factors: (i) near-interface defects,[95] as the device was prepared using Cu-rich $CuGaS_2$ absorbers, and (ii) a negative conduction band offset at the $CuGaS_2$/(Zn,Mg)O interface, owing to the high conduction band minimum of $CuGaS_2$ and the relatively low conduction band minimum of (Zn,Mg)O. While the former limits V_{OC} by reducing the QFLS near the interface and can be mitigated by performing chalcogen treatment,[96] the latter limits V_{OC} by reducing the QFLS and requires a buffer that is better matched to the conduction band minimum of $CuGaS_2$. Nonetheless, this work demonstrates that it is possible to fabricate working solar cells with $CuGaS_2$, although significant effort is required to achieve useful V_{OC} and power conversion efficiencies.

ACKNOWLEDGEMENTS

The authors acknowledge that this research was funded in whole, or in part, by the Luxembourg National Research Fund (FNR), in the framework of the MASSENA project (Grant PRIDE 15/10935404). For the purpose of open access, the author has applied for a Creative Commons Attributions 4.0 International (CC BY 4.0) license to any Author Accepted Manuscript version arising from this submission. We also acknowledge Dr. Mael Guennou for the Raman spectroscopy of the $CuGaS_2$ film.

DATA AVAILABILITY STATEMENT

The data that support the findings of this study are available from the corresponding author upon reasonable request.

ORCID

Damilola Adeleye https://orcid.org/0000-0001-6359-9100
Mohit Sood https://orcid.org/0000-0002-2714-7737
Michele Melchiorre https://orcid.org/0000-0003-0536-907X
Alice Debot https://orcid.org/0000-0003-4176-4077
Susanne Siebentritt https://orcid.org/0000-0001-6522-1427

REFERENCES

1. Albrecht S, Rech B. Perovskite solar cells: on top of commercial photovoltaics. *Nat Energy*. 2017;2(1):16196. doi:10.1038/nenergy.2016.196
2. Al-Ashouri A, Köhnen E, Li B, et al. Monolithic perovskite/silicon tandem solar cell with >29% efficiency by enhanced hole extraction. *Science*. 2020;370(6522):1300-1309. doi:10.1126/science.abd4016
3. Siebentritt S, Weiss T. Chalcopyrite solar cells—state-of-the-art and options for improvement. *Sci China Phys Mech Astronomy*. 2023;66(1): 217301. doi:10.1007/s11433-022-2001-4
4. Barreau N, Bertin E, Crossay A, et al. Investigation of co-evaporated polycrystalline $Cu(In,Ga)S_2$ thin film yielding 16.0% efficiency solar cell. *EPJ Photovoltaics*. 2022;13:17. doi:10.1051/epjpv/2022014
5. NREL. Best research-cell efficiency chart. 2023. Available from: https://www.nrel.gov/pv/cell-efficiency.html
6. Hiroi H, Iwata Y, Adachi S, Sugimoto H, Yamada A. New world-record efficiency for pure-sulfide $Cu(In,Ga)S_2$ thin-film solar cell with cd-free buffer layer via KCN-free process. *IEEE J Photovoltaics*. 2016;6(3): 760-763. doi:10.1109/JPHOTOV.2016.2537540
7. Hiroi H, Iwata Y, Horiguchi K, Sugimoto H. 960-mV open-circuit voltage chalcopyrite solar cell. *IEEE J Photovoltaics*. 2015;6(1):309-312. doi:10.1109/JPHOTOV.2015.2479470
8. Nakamura M, Yamaguchi K, Kimoto Y, Yasaki Y, Kato T, Sugimoto H. Cd-free $Cu(In,Ga)(Se,S)_2$ thin-film solar cell with record efficiency of 23.35%. *IEEE J Photovoltaics*. 2019;9(6):1863-1867. doi:10.1109/JPHOTOV.2019.2937218
9. Siebentritt S, Lomuscio A, Adeleye D, Sood M, Dwivedi A. Sulfide chalcopyrite solar cells––are they the same as selenides with a wider bandgap? *Phys Status Solidi (RRL) Rapid Res Lett*. 2022;16(8):2200126. doi:10.1002/pssr.202200126
10. Shukla S, Sood M, Adeleye D, et al. Over 15% efficient wide-band-gap $Cu(In,Ga)S_2$ solar cell: suppressing bulk and interface recombination through composition engineering. *Joule*. 2021;5(7): 1816-1831. doi:10.1016/j.joule.2021.05.004
11. Bauknecht A, Siebentritt S, Albert J, Lux-Steiner MC. Radiative recombination via intrinsic defects in $Cu_xGa_ySe_2$. *J Appl Phys*. 2001; 89(8):4391-4400. doi:10.1063/1.1357786
12. Rega N, Siebentritt S, Albert J, et al. Excitonic luminescence of $Cu(In,Ga)Se_2$. *Thin Solid Films*. 2005;480:286-290. doi:10.1016/j.tsf.2004.11.079
13. Siebentritt S. Shallow defects in the wide gap chalcopyrite $CuGaSe_2$. In: Siebentritt S, Rau U, eds. *Wide-Gap Chalcopyrites*. Springer Series in Materials Science. Vol.86. Springer; 2006:113-156. doi:10.1007/3-540-31293-5_7
14. Spindler C, Babbe F, Wolter MH, et al. Electronic defects in $Cu(In,Ga)Se_2$: towards a comprehensive model. *Phys Rev Mater*. 2019;3(9): 090302. doi:10.1103/PhysRevMaterials.3.090302
15. Siebentritt S, Igalson M, Persson C, Lany S. The electronic structure of chalcopyrites—bands, point defects and grain boundaries. *Progr Photovoltaics: Res Applic*. 2010;18(6):390-410. doi:10.1002/pip.936
16. Dirnstorfer I, Wagner M, Hofmann DM, Lampert MD, Karg F, Meyer BK. Characterization of $CuIn(Ga)Se_2$ thin films. *Phys Status Solidi (A)*. 1998;168(1):163-175. doi:10.1002/(SICI)1521-396X(199807)168:1%3C163::AID-PSSA163%3E3.0.CO;2-T
17. Wagner M, Dirnstorfer I, Hofmann DM, Lampert MD, Karg F, Meyer BK. Characterization of $CuIn(Ga)Se_2$ thin films. *Phys Status Solidi (A)*. 1998;167(1):131-142. doi:10.1002/(SICI)1521-396X(199805)167:1%3C131::AID-PSSA131%3E3.0.CO;2-F
18. Wagner M, Hofmann DM, Dirnstorfer I, Lampert MD, Karg F, Meyer BK. Characterization of $CuIn(Ga)Se_2$ thin films. *Phys Status Solidi (A)*. 1998;168(1):153-161. doi:10.1002/(SICI)1521-396X(199807)168:1%3C153::AID-PSSA153%3E3.0.CO;2-X

1099159x, 0, Downloaded from https://onlinelibrary.wiley.com/doi/10.1002/pip.3778 by Cochrane Luxembourg, Wiley Online Library on [21/03/2024]. See the Terms and Conditions (https://onlinelibrary.wiley.com/terms-and-conditions) on Wiley Online Library for rules of use; OA articles are governed by the applicable Creative Commons License

19. Zott S, Leo K, Ruckh M, Schock HW. Photoluminescence of polycrystalline $CuInSe_2$ thin films. *Appl Phys Lett*. 1996;68(8):1144-1146. doi:10.1063/1.115704
20. Pohl J, Albe K. Intrinsic point defects in $CuInSe_2$ and $CuGaSe_2$ as seen via screened-exchange hybrid density functional theory. *Phys Rev B*. 2013;87(24):245203. doi:10.1103/PhysRevB.87.245203
21. Shukla S, Adeleye D, Sood M, et al. Carrier recombination mechanism and photovoltage deficit in 1.7-eV band gap near-stoichiometric $Cu(In,Ga)S_2$. *Phys Rev Mater*. 2021;5(5):055403. doi:10.1103/PhysRevMaterials.5.055403
22. Kim S, Nagai T, Tampo H, Ishizuka S, Shibata H. Large open-circuit voltage boosting of pure sulfide chalcopyrite $Cu(In,Ga)S_2$ prepared using Cu-deficient metal precursors. *Progr Photovoltaics: Res Applic*. 2020;28(8):816-822. doi:10.1002/pip.3277
23. Weinhardt L, Fuchs O, Groß D, et al. Band alignment at the CdS/Cu$(In,Ga)S_2$ interface in thin-film solar cells. *Appl Phys Lett*. 2005;86(6):062109. doi:10.1063/1.1861958
24. Merdes S, Mainz R, Klaer J, et al. 12.6% efficient CdS/$Cu(In,Ga)S_2$-based solar cell with an open circuit voltage of 879 mV prepared by a rapid thermal process. *Solar Energy Mater Solar Cells*. 2011;95(3):864-869. doi:10.1016/j.solmat.2010.11.003
25. Merdes S, Sáez-Araoz R, Ennaoui A, Klaer J, Lux-Steiner MC, Klenk R. Recombination mechanisms in highly efficient thin film Zn(S,O)/Cu(In,Ga)S_2 based solar cells. *Appl Phys Lett*. 2009;95(21):213502. doi:10.1063/1.3266829
26. Lomuscio A, Sood M, Melchiorre M, Siebentritt S. Phonon coupling and shallow defects in CuIn S_2. *Phys Rev B*. 2020;101(8):085119. doi:10.1103/PhysRevB.101.085119
27. Massé G. Luminescence of $CuGaS_2$. *J Appl Phys*. 1985;58(2):930-935. doi:10.1063/1.336168
28. Shirakata S, Saiki K, Isomura S. Excitonic photoluminescence in $CuGaS_2$ crystals. *J Appl Phys*. 1990;68(1):291-297. doi:10.1063/1.347131
29. Branch MS, Berndt PR, Leitch AWR, Botha JR, Weber J. Structural and optical characterisation of $CuGaS_2$ thin films grown by MOVPE. *Thin Solid Films*. 2005;480–481:188-194. doi:10.1016/j.tsf.2004.11.084
30. Metzner H, Eberhardt J, Cieslak J, et al. Photoluminescence of epitaxial $CuGaS_2$ on Si(111): model for intrinsic defect levels. *Thin Solid Films*. 2004;451:241-244. doi:10.1016/j.tsf.2003.10.120
31. Shirakata S, Chichibu S. Photoluminescence of $CuGaS_2$ epitaxial layers grown by metalorganic vapor phase epitaxy. *J Appl Phys*. 2000;87(8):3793-3799. doi:10.1063/1.372416
32. Yagi M, Terasako T, Tsuboi N, Iida S. Deep region emissions of $CuGaS_2$ Crystals. *Jpn J Appl Phys*. 1993;32(S3):618. doi:10.7567/JJAPS.32S3.618
33. Eberhardt J, Metzner H, Hahn T, et al. Optical properties of epitaxial $CuGaS_2$ layers on Si(111). *J Phys Chem Solid*. 2003;64(9–10):1781-1785. doi:10.1016/S0022-3697(03)00199-9
34. Branch MS, Berndt PR, Leitch AWR, Botha JR, Weber J. The influence of growth parameters on the structure and composition of $CuGaS_2$ epilayers grown by MOVPE. *Phys B: Condensed Matter*. 2006;376–377:803-807. doi:10.1016/j.physb.2005.12.201
35. Metzner H, Hahn T, Cieslak J, et al. Epitaxial growth of $CuGaS_2$ on Si(111). *Appl Phys Lett*. 2002;81(1):156-158. doi:10.1063/1.1492003
36. Botha JR, Branch MS, Berndt PR, Leitch AWR, Weber J. Defect chemistry in $CuGaS_2$ thin films: a photoluminescence study. *Thin Solid Films*. 2007;515(15):6246-6251. doi:10.1016/j.tsf.2006.12.083
37. Lomuscio A, Melchiorre M, Siebentritt S. Influence of stoichiometry and temperature on quasi Fermi level splitting of sulfide CIS absorber layers. In: *2018 IEEE 7th World Conference on Photovoltaic Energy Conversion (WCPEC) (A Joint Conference of 45th IEEE PVSC, 28th PVSEC & 34th EU PVSEC)*. IEEE; 2018. doi:10.1109/PVSC.2018.8548252
38. Kokta M, Carruthers JR, Grasso M, Kasper HM, Tell B. Ternary phase relations in the vicinity of chalcopyrite copper gallium sulfide. *J Electron Mater*. 1976;5(1):69-89. doi:10.1007/BF02652887
39. Guillen C, Herrero J. $CuInS_2$ and $CuGaS_2$ thin films grown by modulated flux deposition with various Cu contents. *Phys Status Solidi (A)*. 2006;203(10):2438-2443. doi:10.1002/pssa.200622132
40. Guillén C, Herrero J. Characteristics of stacked $CuInS_2$ and $CuGaS_2$ layers as determined by the growth sequence. *Thin Solid Films*. 2007;515(15):5917-5920. doi:10.1016/j.tsf.2006.12.141
41. Binsma J, Giling L, Bloem J. Luminescence of $CuInS_2$: I. The broad band emission and its dependence on the defect chemistry. *JOL*. 1982;27(1):35-53. doi:10.1016/0022-2313(82)90028-X
42. Binsma J, Giling L, Bloem J. Phase relations in the system Cu_2S-In_2S_3. *J Cryst Growth*. 1980;50(2):429-436. doi:10.1016/0022-0248(80)90090-1
43. Bodnar IV, Bodnar IT, Vaipolin AA. Growth and morphology of the $CuGaS_2$, $CuAlSe_2$, $CuGaSe_2$ and $CuInS_2$ ternary compounds. *Crystal Res Technol*. 1984;19(12):1553-1557. doi:10.1002/crat.2170191205
44. Matsushita H, Endo SES, Irie TIT. Thermodynamical properties of I-III-VI2-group chalcopyrite semiconductors. *Jpn J Appl Phys*. 1991;30(6R):1181. doi:10.1143/JJAP.30.1181
45. Rincón C. Deby temperature and melting point in AIBIIIC2VI and AIIBIVC2V chalcopyrite compounds. *Phys Status Solidi (A)*. 1992;134(2):383-389. doi:10.1002/pssa.2211340208
46. Weber M, Scheer R, Lewerenz HJ, Jungblut H, Störkel U. Microroughness and composition of cyanide-treated $CuInS_2$. *J Electrochem Soc*. 2001;149(1):G77. doi:10.1149/1.1424899
47. Bauknecht A, Siebentritt S, Gerhard A, et al. Defects in $CuGaSe_2$ thin films grown by MOCVD. *Thin Solid Films*. 2000;361:426-431. doi:10.1016/S0040-6090(99)00752-X
48. Siebentritt S, Rega N, Zajogin A, Lux-Steiner MC. Do we really need another PL study of $CuInSe_2$? *Phys. Stat. Sol. C*. 2004;1(9):2304-2310.
49. Maeda T, Yu Y, Chen Q, Ueda K, Wada T. Crystallographic and optical properties and band diagrams of $CuGaS_2$ and $CuGa_5S_8$ phases in Cu-poor Cu_2S–Ga_2S_3 pseudo-binary system. *Jpn J Appl Phys*. 2017;56(4S):04CS12. doi:10.7567/JJAP.56.04CS12
50. Klenk M, Schenker O, Alberts V, Bucher E. Preparation of device quality chalcopyrite thin films by thermal evaporation of compound materials. *Semicond Sci Technol*. 2002;17(5):435-439. doi:10.1088/0268-1242/17/5/305
51. Thomere A, Guillot-Deudon C, Caldes MT, et al. Chemical crystallographic investigation on Cu_2S-In_2S_3-Ga_2S_3 ternary system. *Thin Solid Films*. 2018;665:46-50. doi:10.1016/j.tsf.2018.09.003
52. Caballero R, Guillén C. Comparative studies between Cu Ga Se and Cu In Se thin film systems. *Thin Solid Films*. 2002;403:107-111. doi:10.1016/S0040-6090(01)01537-1
53. Ishizuka S, Yamada A, Fons P, Niki S. Texture and morphology variations in $(In,Ga)_2Se_3$ and $Cu(In,Ga)Se_2$ thin films grown with various Se source conditions. *Progr Photovoltaics: Res Applic*. 2013;21(4):544-553. doi:10.1002/pip.1227
54. Chichibu S, Shirakata S, Uchida M, et al. Heteroepitaxial growth of $CuGaS_2$ layers by low-pressure metalorganic chemical vapor deposition. *Jpn J Appl Phys*. 1995;34(8R):3991. doi:10.1143/JJAP.34.3991
55. Gdowski G, Madix R. The effect of sulfur on co adsorption/desorption on Pt(S)-[9(111) $\times$ (100)]. *Surf Sci*. 1982;115(3):524-540. doi:10.1016/0039-6028(82)90385-5
56. Guillén C, Herrero J, Gutiérrez MT, Briones F. Structure, morphology and optical properties of $CuInS_2$ thin films prepared by modulated flux deposition. *Thin Solid Films*. 2005;480:19-23. doi:10.1016/j.tsf.2004.11.027
57. Siebentritt S, Rau U, Gharabeiki S, et al. Photoluminescence assessment of materials for solar cell absorbers. *Faraday Discuss*. 2022;239:112-129. doi:10.1039/D2FD00057A
58. Klenk R, Walter T, Schock HW, Cahen D. A model for the successful growth of polycrystalline films of $CuInSe_2$ by multisource physical vacuum evaporation. *Adv Mater*. 1993;5(2):114-119. doi:10.1002/adma.19930050209

1099159x, 0, Downloaded from https://onlinelibrary.wiley.com/doi/10.1002/pip.3778 by Cochrane Luxembourg, Wiley Online Library on [21/03/2024]. See the Terms and Conditions (https://onlinelibrary.wiley.com/terms-and-conditions) on Wiley Online Library for rules of use; OA articles are governed by the applicable Creative Commons License

59. Botha JR, Branch MS, Leitch AWR, Weber J. Radiative defects in $CuGaS_2$ thin films. *Phys B: Condensed Matter*. 2003;340–342:923-927. doi:10.1016/j.physb.2003.09.203
60. Witte W, Abou-Ras D, Albe K, et al. Gallium gradients in Cu(In,Ga)Se_2 thin-film solar cells. *Progr Photovoltaics: Res Applic*. 2015;23(6):717-733. doi:10.1002/pip.2485
61. Lomuscio A, Rödel T, Schwarz T, et al. Quasi-Fermi-level splitting of Cu-poor and Cu-rich Cu in S_2 absorber layers. *Phys Rev Appl*. 2019;11(5):054052. doi:10.1103/PhysRevApplied.11.054052
62. Siebentritt S, Gütay L, Regesch D, Aida Y, Deprédurand V. Why do we make Cu(In,Ga)Se_2 solar cells non-stoichiometric? *Solar Energy Mater Solar Cells*. 2013;119:18-25. doi:10.1016/j.solmat.2013.04.014
63. van der Ziel JP, Meixner AE, Kasper HM, Ditzenberger JA. Lattice vibrations of $AgGaS_2$, $AgGaSe_2$, and $CuGaS_2$. *Phys Rev B*. 1974;9(10):4286-4294. doi:10.1103/PhysRevB.9.4286
64. Sugai S. Resonant Raman scattering in $CuGaS_2$. *J Physical Soc Japan*. 1977;43(2):592-599. doi:10.1143/JPSJ.43.592
65. Rincon C, Ramirez F. Lattice vibrations of $CuInSe_2$ and $CuGaSe_2$ by Raman microspectrometry. *J Appl Phys*. 1992;72(9):4321-4324. doi:10.1063/1.352195
66. Wakita K, Hirooka H, Yasuda S, Fujita F, Yamamoto N. Resonant Raman scattering and luminescence in $CuInS_2$ crystals. *J Appl Phys*. 1998;83(1):443-447. doi:10.1063/1.366658
67. Li X, Li J, Wang K, et al. Pressure and temperature-dependent Raman spectra of MoS_2 film. *Appl Phys Lett*. 2016;109(24):242101. doi:10.1063/1.4968534
68. Pankove JI. *Optical Processes in Semiconductors*. Dover Publications; 1975.
69. Spindler C, Galvani T, Wirtz L, Rey G, Siebentritt S. Excitation-intensity dependence of shallow and deep-level photoluminescence transitions in semiconductors. *J Appl Phys*. 2019;126(17):175703. doi:10.1063/1.5095235
70. Schmidt T, Lischka K, Zulehner W. Excitation-power dependence of the near-band-edge photoluminescence of semiconductors. *Phys Rev B*. 1992;45(16):8989-8994. doi:10.1103/PhysRevB.45.8989
71. Spindler C. *Optical Detection of Deep Defects in Cu(In,Ga)Se_2*. University of Luxembourg; 2018.
72. Cardona M, Peter YY. *Fundamentals of Semiconductors*. Vol. 619. Springer; 2005.
73. Hopfield JJ, Thomas DG, Gershenzon M. Pair spectra in GaP. *Phys Rev Lett*. 1963;10(5):162-164. doi:10.1103/PhysRevLett.10.162
74. Yu PW. Excitation-dependent emission in Mg-, Be-, Cd-, and Zn-implanted GaAs. *J Appl Phys*. 1977;48(12):5043-5051. doi:10.1063/1.323631
75. Tanaka K, Uchiki H, Iida S, Terasako T, Shirakata S. Biexciton luminescence from $CuGaS_2$ bulk single crystals. *Solid State Commun*. 2000;114(4):197-201. doi:10.1016/S0038-1098(00)00035-1
76. Binsma J, Giling L, Bloem J. Luminescence of $CuInS_2$: II. Exciton and near edge emission. *JOL*. 1982;27(1):55-72. doi:10.1016/0022-2313(82)90029-1
77. Shay JL, Tell B, Kasper HM. Visible stimulated emission in ternary chalcopyrite sulfides and selenides. *Appl Phys Lett*. 1971;19(9):366-368. doi:10.1063/1.1653955
78. Tell B, Shay JL, Kasper HM. Electrical properties, optical properties, and band structure of $CuGaS_2$ and $CuInS_2$. *Phys Rev B*. 1971;4(8):2463-2471. doi:10.1103/PhysRevB.4.2463
79. Yu PW, Downing DL, Park YS. Electrical properties of $CuGaS_2$ single crystals. *J Appl Phys*. 1974;45(12):5283-5288. doi:10.1063/1.1663231
80. Rincón C, González J. Acoustic deformation potentials in AIBIIICVI2 chalcopyrite semiconductors. *Phys Rev B*. 1989;40(12):8552-8554. doi:10.1103/PhysRevB.40.8552
81. Bellabarba C, Gonzalez J, Rincon C. Optical-absorption spectrum near the exciton band edge in $CuGaS_2$ at 5 K. *Phys Rev B Condens Matter*. 1996;53(12):7792-7796. doi:10.1103/PhysRevB.53.7792
82. Tell B, Kasper HM. Electrical properties of $CuGaS_2$. *J Appl Phys*. 1973;44(11):4988-4990. doi:10.1063/1.1662075
83. Sharma R, Rodriguez S. Theory of excitons bound to ionized impurities in semiconductors. *Phys Rev*. 1967;153(3):823-827. doi:10.1103/PhysRev.153.823
84. Hopfield J. The quantum chemistry of bound exciton complexes. In: Hulin M, ed. *Proceedings of the 7th International Conference on the Physics of Semiconductors*. Dunod; 1964:725-735.
85. Haynes JR. Experimental observation of the Excitonic molecule. *Phys Rev Lett*. 1966;17(16):860-862. doi:10.1103/PhysRevLett.17.860
86. Atzmüller H, Fröschl F, Schröder U. Theory of excitons bound to neutral impurities in polar semiconductors. *Phys Rev B*. 1979;19(6):3118-3129. doi:10.1103/PhysRevB.19.3118
87. Botha JR, Branch MS, Chowles AG, Leitch AWR, Weber J. Photoluminescence of vacuum-deposited $CuGaS_2$ thin films. *Phys B: Condensed Matter*. 2001;308:1065-1068. doi:10.1016/S0921-4526(01)00848-1
88. Huang K, Rhys A, Mott NF. Theory of light absorption and non-radiative transitions in *F*-centres. *Proc R Soc Lond A Math Phys Sci*. 1950;204(1078):406-423.
89. Reshchikov MA, Morkoç H. Luminescence properties of defects in GaN. *J Appl Phys*. 2005;97(6):5-19. doi:10.1063/1.1868059
90. Alkauskas A, McCluskey MD, Van de Walle CG. Tutorial: defects in semiconductors—combining experiment and theory. *J Appl Phys*. 2016;119(18):181101. doi:10.1063/1.4948245
91. Spindler C, Regesch D, Siebentritt S. Revisiting radiative deep-level transitions in $CuGaSe_2$ by photoluminescence. *Appl Phys Lett*. 2016;109(3):032105. doi:10.1063/1.4959557
92. Gonzalez J, Moya E, Chervin J. Anharmonic effects in light scattering due to optical phonons in $CuGaS_2$. *Phys Rev B*. 1996;54(7):4707-4713. doi:10.1103/PhysRevB.54.4707
93. Zacks E, Halperin A. Dependence of the peak energy of the pair-photoluminescence band on excitation intensity. *Phys Rev B*. 1972;6(8):3072-3075. doi:10.1103/PhysRevB.6.3072
94. Shockley W, Queisser HJ. Detailed balance limit of efficiency of p-n junction solar cells. *J Appl Phys*. 1961;32(3):510-519. doi:10.1063/1.1736034
95. Sood M, Urbaniak A, Kameni Boumenou C, et al. Near surface defects: cause of deficit between internal and external open-circuit voltage in solar cells. *Progr Photovoltaics: Res Applic*. 2022;30(3):263-275. doi:10.1002/pip.3483
96. Sood M, Lomuscio A, Werner F, et al. Passivating surface defects and reducing interface recombination in $CuInS_2$ solar cells by a facile solution treatment. *Solar RRL*. 2021;5(4):2100078. doi:10.1002/solr.202100078

How to cite this article: Adeleye D, Sood M, Melchiorre M, Debot A, Siebentritt S. Composition dependence of electronic defects in $CuGaS_2$. *Prog Photovolt Res Appl*. 2024;1-18. doi:10.1002/pip.3778

1099159x, 0, Downloaded from https://onlinelibrary.wiley.com/doi/10.1002/pip.3778 by Cochrane Luxembourg, Wiley Online Library on [21/03/2024]. See the Terms and Conditions (https://onlinelibrary.wiley.com/terms-and-conditions) on Wiley Online Library for rules of use; OA articles are governed by the applicable Creative Commons License